Magnetic Resonance Elastography Of Anisotropic Materials Under Pre-Strained Boundary Conditions

BY

LUCA LEONI
B.S. , Politecnico di Milano, Milan, Italy, 2018

THESIS

Submitted as partial fulfillment of the requirements
for the degree of Master of Science in Bioengineering
in the Graduate College of the
University of Illinois at Chicago, 2020

Chicago, Illinois

Defense Committee:

Thomas J. Royston, Chair and Advisor
Dieter Klatt
Pasquale Vena, Politecnico di Milano

ACKNOWLEDGMENTS

First, I would like to express sincere gratitude to Prof. Thomas J. Royston for welcoming me aboard the Acoustics and Vibrations Laboratory and introducing me to an innovative and interesting diagnostic tool as MRE is.

I am grateful to Prof. Dieter Klatt, who has been enlightening with his insights into elastographic subject, and to Prof. Pasquale Vena for his help and willingness throughout in the Double Degree program.

A huge “thank you” to Martina Guidetti and Harish Palnitkar, who have been helping decisively in the development of ideas for this thesis project and in correct use of many of the tools I utilized.

Thank you to the whole Acoustics and Vibrations Laboratory, Chiara Gambacorta, Bekah Allen, Joseph Crutison, Lara Nammari, Joshua Smejkal, for having provided precious advices and been amazing colleagues.

Thanks also to Gio who helped me in the CAD design.

Last but not least, thank you Ciro for being a great journey mate in the Chi-town experience, and thanks to everyone I had the chance meet and share moments of this unique time.

A special thank to all those directly dealing with coronavirus, which did not allow me to carry out as many experiments as I expected.

NSF grant number 1852691 and NIH grant number AR071162 are acknowledged.

Finally, and most importantly, I would like to thank the other four Lions.

LL

TABLE OF CONTENTS

CHAPTER **PAGE**

TABLE OF CONTENTS (continued)

LIST OF TABLES

LIST OF FIGURES

FIGURE **PAGE**

FIGURE **PAGE**

SUMMARY

Magnetic Resonance Elastography (MRE) is a noninvasive diagnostic imaging technique. Developed recently, it is capable to assess tissues' viscoelastic properties mechanically stimulating them and exploiting Magnetic Resonance Imaging (MRI) motion-sensitive gradients. MRE is promising for applications on a wide range of organs and tissues, including skeletal muscles.

Variations in viscoelastic properties of tissues might be sign of an ongoing pathology in a tissue. In the muscular case, diseases affecting those properties could be spasticity, Duchenne muscular dystrophy, and hyperthyroidism. Not only MRE is practical to detect early stages of the specified syndromes, but we hypothesize that it also can be employed for a deep understanding of how active and passive tensions influence apparent muscle viscoelastic features.

The present work aims at investigating how passive pre-tension determines alterations of apparent shear stiffness in an Ecoflex™ phantom mimicking skeletal muscle fibrous architecture and transversely isotropic properties at different axial elongation values. Such analysis is performed both experimentally and computationally. Experimental MRE in pre-strained boundary conditions requires the design on SolidWorks and the machining of a MR suitable setup simultaneously capable to axially elongate the cited phantom, and to provide it with mechanical shear excitation. Magnetic Resonance Elastography acquisitions are made with an Agilent 9.4 T imaging system for which the setup is specifically designed.

Finite Element Analysis (FEA) is implemented on COMSOL Multiphysics, after having built a phantom model in SolidWorks. The FE virtual experiment, by means of a direct problem, simulates the practical trials, imposing progressively larger pre-strain boundary conditions to the phantom model.

An analysis of the wave images obtained enables to understand how frequency dependent viscoelastic parameters and axial pre-strain influence propagation of shear waves.

CHAPTER 1

INTRODUCTION

A large wealth of diagnostic information about biological tissues has been obtained habitually from palpation, a practice perpetrated to assess mechanical properties of organs at macroscopic level. Palpation is a traditional diagnostic tool determining qualitatively macroscopic stiffness of an organ by means of its response to applied deformation. It has a high sensitivity, since shear stiffness of the diverse tissues and organs widens over a range of eight orders of magnitude. However, the mentioned procedure includes some limitations: firstly, it estimates the mechanical properties only qualitatively; secondly, the diagnosis is restricted to body surface and it does not allow deep organs detection. Finally, palpation is subject to a relevant intra- and inter-operator dependence [1].

The alteration of elastic and viscous properties has been identified as a possible early sign of the progression of a variety of pathologies in different body tissues. None of the most widespread imaging techniques are able to assess the features of a tissue that palpation enables to aim at [1]. In the past decades, elastographic imaging methods were exploited to investigate eventual relations between variation in mechanical properties and specific pathological conditions. In fibrotic liver, the grade of the disease was quantitatively determined with the shear modulus of the organ, resolved through post-processing of multiple Magnetic Resonance Elastography (MRE) scans [2][3]. More broadly, many other fibrotic pathologies could be assessed with MRE, including pulmonary and endomyocardial fibrosis. Recent studies showed that neurodegenerative diseases, e.g. Alzheimer’s Disease, Parkinson’s Disease and normal aging, might change brain parenchyma elastic properties, induced by a reduction in stiffness of neurons [4][5]. Also, increased arterial stiffness characterizes a rising morbidity and cardiovascular mortality in hypertensive subjects [6]. Furthermore, pathologies of the skeletal muscle could be monitored through the MRE, including spasticity, Duchenne muscular dystrophy and fibromyalgia [7][8][9].

Among the range of elastographic modalities, dynamic MRE is a recent non-invasive in vivo elasticity imaging technique, that can be interpreted as a “remote palpation”. Indeed, palpation is emulated by a harmonic mechanical stimulation provided by an actuator disposed as adjacent as possible to the organ of interest (Figure 1). MRE allows to depict propagation of mechanical waves that the actuator generates within biological tissues, through the analysis of oscillation-related displacement. Such investigation is performed by means of a Magnetic Resonance (MR) motion sensitive gradient, which enables to obtain phase contrast or wave images within cross sections of the tissue. From the wave images it is then possible to build a quantitative map of the local shear modulus in a tissue, or elastogram [1][10].

The harmonic mechanical actuation is essential in an MRE scan since it acts as source of shear waves propagating into the viscoelastic medium. From the variations in wavelength of the geometrically focused propagating mechanical waves it is possible to study the stiffness distribution within the tissue. The stiffer the tissue, the shorter the local displacement, the longer the wavelength, therefore the faster the wave speed will be in the direction of propagation [10].

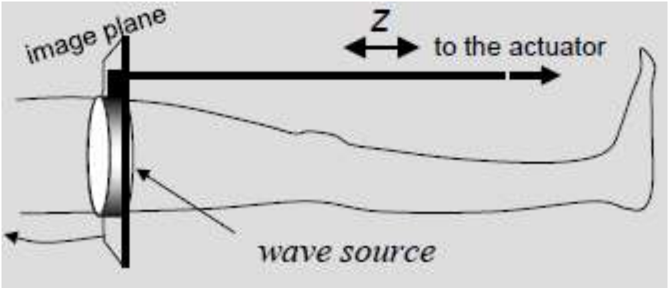

Figure 1: Schematic of experimental setup for transmission of shear waves in an MRE scan. The wave source moves harmonically along the longitudinal (z) axis. Provided by Prof. Dieter Klatt.

MRE presents some benefits to both patient and clinician in comparison with palpation and other traditional diagnostic techniques, such as percutaneous biopsy. Foremost, it is completely noninvasive and does not harm the patient. In contrast with biopsy, which allows only to examine a portion of an organ, MRE returns a representation of the shear modulus distribution in the whole tissue [11]. MRE represents also a quantitative tool in determining the shear stiffness, going far beyond the qualitative assessment typical of palpation. Moreover, MRE allows to detect deep tissues stiffness, differently from palpation that only can assess superficial organs.

While MRE applied to many different organs has been widely treated in literature, with particular reference to brain, breast and liver [1], not much is known about skeletal muscle in vivo viscoelastic properties and their relationship with muscular microstructure, both in physiological and pathological conditions. A deeper understanding of the dynamics of propagation of mechanical waves within the muscle would enable to determine the possible linking between the microstructure of a skeletal muscle and its viscous and elastic features. In such context, the role of passive and active components of the muscular tissue in establishing the shear modulus of a passively strained skeletal muscle should be further investigated. This whole procedure would then allow to gain insights on muscle biomechanics in a healthy state and in disease [10].

The presented work has a multiple aim: firstly, to design, build and test a MR-suitable experimental setup able both to longitudinally prestress the specimen to study and to apply a mechanical stimulation to the specimen itself; secondly, to investigate the influence of the longitudinal pretension on the propagation of mechanical waves inside a nonhomogeneous transversely isotropic muscle-mimicking phantom. Such analysis is performed both experimentally and computationally. The first step consists in designing the mechanical setup on Solidworks (Dassault Systèmes Solidworks Corporation, Delaware, U.S., 2019) software, with dimensional constraints related to the internal diameter (ID) of the MRI bore. Then, a process to validate the effectiveness of the setup in transmitting the mechanical harmonic excitation to a silicone cylindrical phantom is undergone. MRE scans and postprocessing of the acquired data are performed to visualize the propagation of mechanical waves along the cross-section of the phantom. The underlying hypothesis is that under the effect of pre-tension, compression waves and not shear waves are those which propagate within the phantom. Moreover, an increase in shear stiffness of the transversely isotropic specimen would yield an enlargement of the wavelength. The hypotheses are tested through practical MRE experiments, with an Agilent 9.4 T magnetic coil (Agilent Technologies Inc., Santa Clara, CA, USA), and through COMSOL Multiphyiscs 5.3a (Stockholm, Sweden) MRE computational simulations. Longitudinal pre-strain boundary conditions applied in COMSOL mimic those imposed with the experimental setup, as well as the mechanical properties of the material model in COMSOL resemble the Ecoflex™ phantom used to simulate skeletal muscle. The Finite Element Analysis (FEA) for pre-elongated MRE could then be validated and used to study mechanical wave propagation in more realistic phantom geometries.

CHAPTER 2

MAGNETIC RESONANCE ELASTOGRAPHY

Magnetic Resonance Elastography (MRE) bases the determination of mechanical properties of the subject tissue on the renowned relationship linking applied stress and strain through elastic moduli. Through the analysis of tissue motion due to propagation of mechanical waves, MRE allows to reconstruct wave patterns within the tissue itself and therefore the spatial distribution of strain. Data on coherent tissue movement is encoded in the phase of the MRI complex signal [12]. Then, by postprocessing signal phase, mechanical properties of the tissue can be estimated through an inversion algorithm. This coincides with the final step of the elastographic diagnosis process and returns a shear stiffness map of the sample.

MRE is characterized by three fundamental components, enabling to collect information on viscous and elastic features of tissues. The first component is the mechanical excitation, the second involves acquisition of the wave images and the last one is the whole process determining the shear modulus in the Region Of Interest (ROI) of the tissue.

2.1 <u>Mechanical excitation</u>

Mechanical excitation is provided by an actuator usually positioned as adjacent as possible to the tissue of interest. To present day, the main kinds of drivers having been exploited to send waves into the sample include electromechanical, piezoelectric and ultrasound based drivers [1]. The common purpose of all these actuators is to apply a single or multiple frequencies stress to the organ to detect and consequently generate geometrically focused mechanical waves, propagating into the organ itself (Figure 2).

The range of frequencies the harmonic mechanical excitation may vary between 10 Hz and 16 KHz. Such frequencies match roughly the audible frequency range. The choice could depend both on the tissue composition on the type of waves the study aims at visualizing [13][14][15]. There is a tradeoff between the spatial resolution, proportional to the mechanical excitation frequency, and the distance the waves can travel before becoming undetectable. This is due to the larger damping high frequency waves experience in biological tissues with respect to low frequency waves. Therefore, higher frequencies allow for an improved spatial resolution, though they are attenuated in a shorter distance in comparison with lower frequency waves: a compromise must be established between the Signal to Noise Ratio (SNR) and the spatial resolution of the final image.

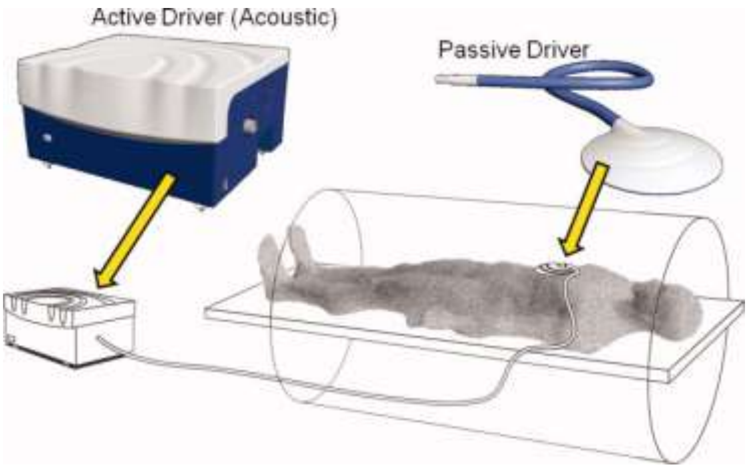

Figure 2: Diagram of a generic mechanical actuator, suitable with MRI system. Provided by Prof. Dieter Klatt from [16].

The external drivers use an electrical signal created by a signal generator triggered by and synchronized to the MR pulse sequence. An audio amplifier amplifies the signal before this enters the actuator [1].

The presented project aims at developing an MRI suitable experimental setup capable of generating and transmitting a longitudinally axisymmetric mechanical excitation. A piezoelectric driver (Physik Instrumente) is used to harmonically move a structure that will transmit said movement to the test sample.

2.2 Wave images acquisition

The most differentiating feature of MRE from all the other traditional imaging techniques is the capability to depict waves propagating in time and space within a material. A Motion Encoding Gradient (MEG) is included among the usual MRI gradients (Slice Selection, Phase Encoding, Frequency Encoding [12]) with the specific purpose of encoding in the phase of the complex MR image the harmonic vibration of single voxels during a scan.

MEG can be imposed along a desired direction to detect the vibratory motion of the sample in that same direction. It is switched on by a trigger signal during Frequency Encoding phase, just before the readout of an MRI scan, and must be synchronized to the harmonic mechanical excitation from the external driver, both having identical frequency. MEG has a sinusoidal or trapezoidal shape, but in some cases, it could be a step function. It is fundamental that the shape is bipolar and symmetric, to allow the phase difference imaging, which will be explained further on. Usually, the start time of the MEG is indicated with the letter s. MEG lasts for a specified time $\tau_k = 2\pi q/\omega_k$, with q being the number of MEG cycles and ω_k the angular frequency in rad/s of the MEG (Figure 3).

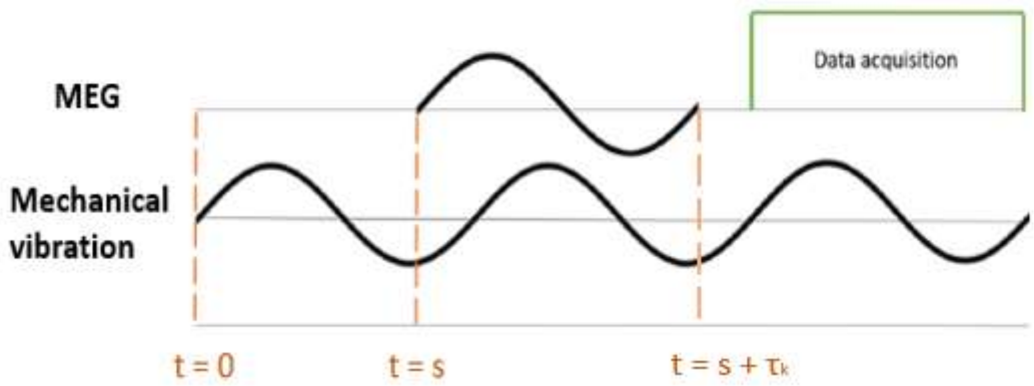

Figure 3: Motion Encoding Gradient (MEG) must be synchronized with mechanical vibration. The trigger signal activates the MEG at time t = s so that MEG is synchronized with harmonic mechanical excitation. Thus, both signals must have the same frequency.

Having the MEG an initial phase $\theta_k = -\,\omega_k s$, one can define the expression for a harmonic Motion Encoding Gradient $K(t)$:

$$K(t) = K_0 \sin\,(\omega_k t + \theta_k) \qquad (2.1)$$

The vibration displacement at the n^th^ excitation frequency can be represented by a sinusoidal function as follows:

$$u_n(t, \boldsymbol{r}) = Y_n(\boldsymbol{r}) \sin\,(\omega_n t + \theta_n) \qquad (2.2)$$

with $u(t, \boldsymbol{r}) = \sum_n u_n(t, \boldsymbol{r})$ in case of multifrequency stimulation. The amplitude of the driver-induced displacement Y_n is commonly in the order of μm [17].

The motion of the tissue is encoded into the phase of the transverse magnetization of spins M_T. Therefore, the phase ϕ of M_T will be a function of both MEG start time s and position $\boldsymbol{r}$:

$$\phi(s, \boldsymbol{r}) = \int_s^{s+\tau_k} \omega_L \, dt = \gamma \int_s^{s+\tau_k} B(t, \boldsymbol{r}) \, dt = \gamma \int_s^{s+\tau_k} K(t) u(t, \boldsymbol{r}) \, dt \qquad (2.3)$$

where ω_L is the Larmor frequency, γ the gyromagnetic ratio, $B(t, \boldsymbol{r})$ the magnetic field. Solving the time integral, the following expression for the phase can be found:

$$\phi_n(s, \boldsymbol{r}) = \phi_n^0 \sin(\omega_n s + \theta_n + \Delta\theta_n) \qquad (2.4)$$

with ϕ_n^0 (a term containing the amplitude of the vibratory motion: $\phi_n^0 = 2\gamma K_0 \frac{\omega_k Y_n \sin\,(q\pi \frac{\omega_n}{\omega_k})}{\omega_n^2 - \omega_k^2}$) and ω_n being constants, $\Delta\theta_n$ the constant phase shift, and θ_n, namely the initial phase of the harmonic mechanical excitation, the only unknown to be identified. Similarly to mechanical vibration displacement, the summation upon n of each frequency-associated phase returns the total value of the transversal magnetization phase:

$$\phi(s,\boldsymbol{r}) = \sum_n \phi_n(s,\boldsymbol{r}) \tag{2.5}$$

A Discrete Fourier Transform (DFT) of $\phi(s,\boldsymbol{r})$ is necessary to pass from time to frequency domain in the scenario of a multifrequency signal. As in every sampling process, the Nyquist frequency must be known so to effectively apply the Shannon theorem. To visualize the displacement of the tissue in meters caused by propagation of the wave at each stimulation frequency, the encoding efficiency parameter ξ_n is used:

$$\xi_n = \frac{\phi_n^0}{Y_n} \tag{2.6}$$

Encoding efficiency indicates how many phase radians are necessary to encode one meter of displacement. Such parameter scales phase image data from radians to micrometers of displacement. At this stage, then, a complex wave image $U(\omega,\boldsymbol{r})$ is obtained: that is a picture showing the acoustic wave propagating in a specific direction within the sample (Figure 4).

$$\boxed{\phi(s,\boldsymbol{r})} \xrightarrow{DFT} \boxed{\phi(\omega,\boldsymbol{r})} \xrightarrow{\xi} \boxed{U(\omega,\boldsymbol{r})}$$

Figure 4: Block diagram of data processing from time to frequency domain through the DFT, and scaling of phase data in rad/s to actual displacement data in m.

To capture snapshots the propagation of the wave in time, a phase offset between MEG and mechanical stimulation must be imposed. Then, different MR acquisitions are performed at various phase offsets (usually four or eight) equally spaced within a wave period and Discrete Fourier Transform will be performed at such time steps [1].

Equation (2.4) states a direct proportionality between the phase of the harmonically vibrating voxel and its displacement. The phase image in this way obtained is also defined wave image. Two images at opposite MEG polarity are caught and a phase difference image is calculated to delete contributions to phase which are not directly related to motion. Consequently, the measure of motion in an organ or tissue within a Magnetic Resonance image phase is commonly known as phase-contrast imaging [18][19].

The analysis of how MRE is developed in the precedent paragraphs assumes an intravoxel coherent motion of protonic spins [12]. In MRE, as well as in Flow MRI, $U(\omega, \boldsymbol{r})$ refers to the displacement of a single isochromat (i.e. voxel) caused by the wave propagation. Within one voxel, the individual spins precess in phase, or coherently. Their relative positions remain constant, while the voxel moves harmonically with the mechanical stimulation (Figure 5). Thus, the macroscopic magnetization vector of one voxel is maximum. MRE encodes the vibratory movement of every voxel: the displacement is calculated from the phase shift contribution of each precessing spin to the entire isochromat. Indeed, displacement and tissue mechanical vibration phase are directly proportional as stated by equation (2.4) [1].

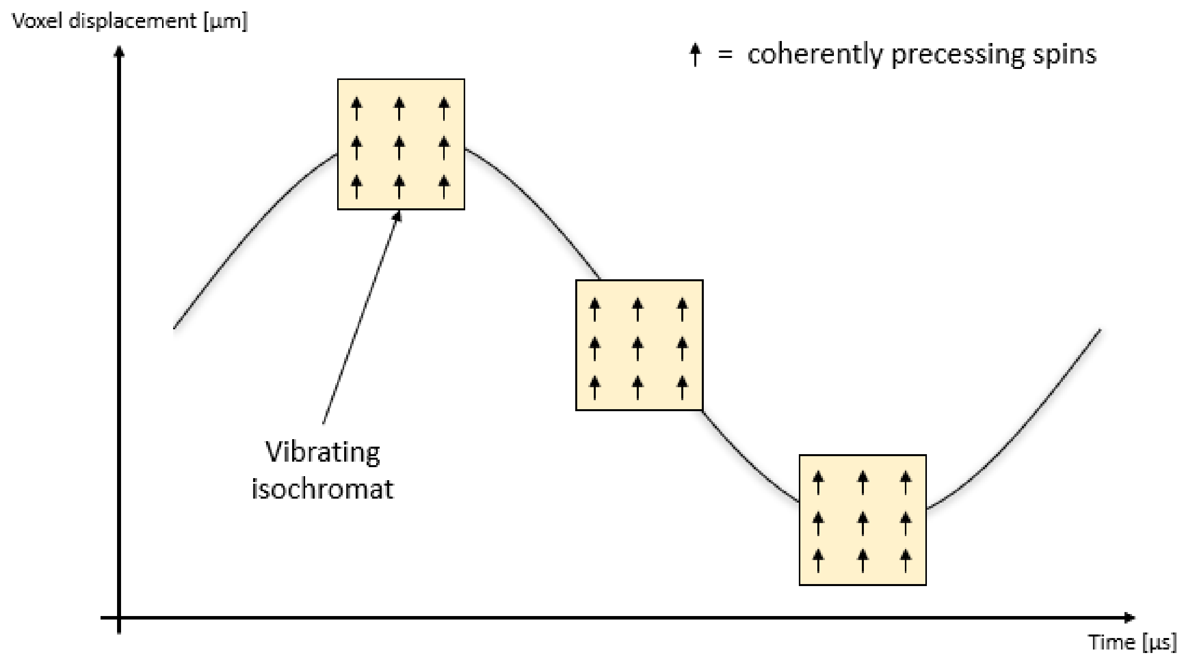

Figure 5: Intravoxel coherent motion of protonic spins. While the spins, represented by the black arrows, precess coherently within one voxel maximizing voxel’s macroscopic magnetization, the voxel itself oscillates driven by the external mechanical stimulation.

2.3 Determination of mechanical parameters

Shear stiffness can be recovered from collected data about the displacement induced by external mechanical excitation. The estimation of shear stiffness is quantitatively performed exploiting equations of motion, which describe how the wave propagates under certain physical and geometrical assumptions (e.g. isotropy, homogeneity, elasticity, linearity). Postprocessing the obtained shear wave images enables to get the elastograms: they are maps depicting the distribution of the complex shear stiffness of the tissue [10][20]. Elastograms are built up knowing that shear modulus can be calculated from wave phase velocity, that is directly proportional to local values of the propagating wavelength.

Chapter number 3 of the presented work is dedicated to a broader dissertation of wave propagation, determination of shear stiffness and postprocessing in MRE to obtain elastograms.

CHAPTER 3

MECHANICAL WAVES PROPAGATION AND INVERSE PROBLEM

Since MRE is a diagnostic tool based on the propagation of mechanical waves in a biological tissue, an analysis about the different kinds of mechanical waves and their propagation dynamics is rather inevitable. In the present chapter, an overview on how waves travel in a continuum, isotropic first and anisotropic then, is due, together with the mathematical algorithm to esteem the shear modulus of the sample under investigation.

First, the presented dissertation considers the medium the waves propagate in as a continuum. Therefore, mass density and elastic moduli parameters are distributed. Moreover, a wave point source produces waves traveling outwards in the space, determining the three-dimensionality of the problem.

Usually, wave types are defined from their propagation modality, the composition and physical features of the medium, and the presence of boundaries to the medium itself. In the case of an isotropic sample, the most relevant kinds of mechanical wave spreading are compression or longitudinal waves, and shear or transverse waves. Other typologies of waves can be generated by the reflection imposed by a boundary: Love and Rayleigh waves are among them [21].

As discussed in the previous chapter, MRE detects primarily cyclic displacement induced by propagation of shear waves only [10], excluding the contribution given by compression waves. While longitudinal waves travel at a speed of 1500 m/s in a soft biological tissue, transverse waves propagate at a rate of two or three orders of magnitude lower: their speed amplitude can range from 1 m/s to 10 m/s depending on input vibration frequency [22][23]. As a Magnetic Resonance Imaging technique, MRE is not capable of capturing the propagation of compression waves. Their spreading at higher frequencies in a soft tissue is driven by bulk modulus, which is subject to a very modest variation within biological tissues. Likewise, at lower frequencies, due to their excessive wavelength, about the order of meters for frequencies below 1 kHz, compression waves cannot be caught within the ROI during a scan [24]. Thus, an algorithm including a step to remove compression wave contribution is necessary. Such passage coincides with the application of curl operator to the wave equation or of a high pass spatial filter.

3.1 Definition of compression and shear waves

Both compression and shear waves can be described by an expression to be derived directly from Navier's equation, made some assumptions about the continuum first. Considering a linear, elastic, homogeneous, isotropic medium, Navier's equation can be written as (neglecting body forces):

$$\rho \frac{\partial^2 \boldsymbol{u}}{\partial t^2} = (\lambda + \mu)\boldsymbol{\nabla\nabla u} + \mu \boldsymbol{\nabla}^2 \boldsymbol{u} \tag{3.1}$$

where ρ is mass density (kg/m^3), $\boldsymbol{u}$ is the displacement (commonly in μm), t is time, λ and μ are 1st and 2nd Lamé parameters, respectively. Due to homogeneity of the sample, λ and μ are independent of position [25].

A longitudinal wave can be defined as:

$$\boldsymbol{u}(\boldsymbol{r}, t) = u_0 \exp\,[i\omega\left(t - \frac{\boldsymbol{n}\cdot\boldsymbol{r}}{c_p}\right)]\boldsymbol{e}_{\parallel \boldsymbol{n}} \tag{3.2}$$

A transverse wave can be expressed as follows:

$$\boldsymbol{u}(\boldsymbol{r}, t) = u_0 \exp\,[i\omega\left(t - \frac{\boldsymbol{n}\cdot\boldsymbol{r}}{c_s}\right)]\boldsymbol{e}_{\perp \boldsymbol{n}} \tag{3.3}$$

In (3.2) and (3.3), $\boldsymbol{r}$ coincides with position vector ($\boldsymbol{r} = [x_1 \quad x_2 \quad x_3]^T$), u_0 expresses the amplitude of the oscillation, i is the imaginary unit, ω the angular frequency (rad/s), $\boldsymbol{n}$ the wave normal vector, c_p and c_s are phase speeds in m/s (where *p* stands for primary wave and *s* for shear or secondary wave), $\boldsymbol{e}_{\parallel \boldsymbol{n}}$ and $\boldsymbol{e}_{\perp \boldsymbol{n}}$ indicate the unit vector parallel and perpendicular to the direction of wave propagation, respectively. Indeed, in compression waves the vibration is parallel to the direction the wave travels along, whereas in transverse waves polarization is orthogonal to propagation direction.

Both equations (3.2) and (3.3) represent a plane wave solution for Navier's equation (3.1). The direction of the motion, therefore the direction the oscillation happens along, establishes whether the wave is longitudinal or transversal.

The phase speed of a wave is directly proportional to its wavelength, as the following holds:

$$c = l\frac{\omega}{2\pi} \tag{3.4}$$

With l being the wavelength (m).

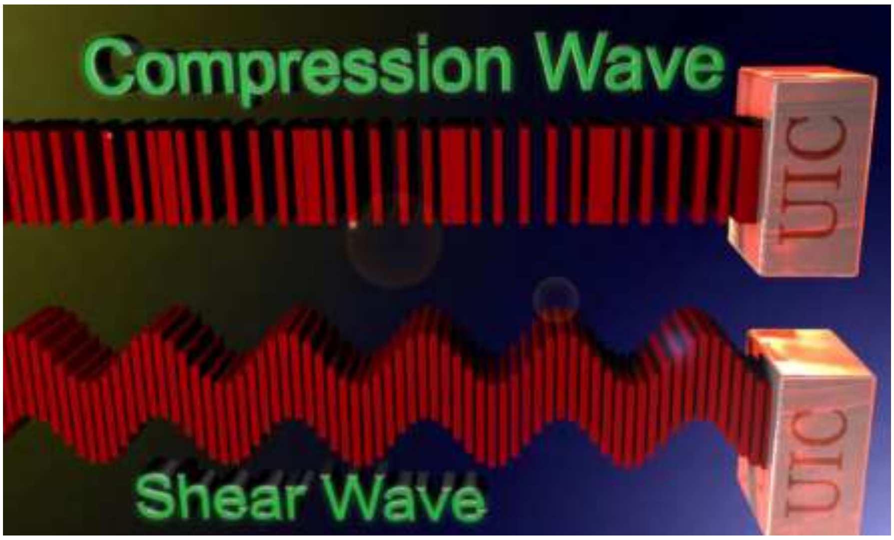

Figure 6: Snapshot of propagation of the two main types of waves in a soft biological tissue: compression and shear waves. Compression waves are characterized by oscillation in the same direction of propagation, while shear waves have vibration polarized orthogonally to wave normal. Provided by T. Kaya Yasar and Prof. Dieter Klatt.

Substituting equations (3.2) and (3.3) in Navier's equation (3.1) and knowing the direction the wave propagates in, one can determine phase speeds for each type of wave. Longitudinal waves phase speed would then be

$$c_p = \sqrt{\frac{\lambda + 2\mu}{\rho}} \tag{3.5}$$

Similarly, transverse waves phase speed acquires the following expression

$$c_s = \sqrt{\frac{\mu}{\rho}} \tag{3.6}$$

The quantitative difference between λ and μ is about four orders of magnitude in soft biological tissues ($\lambda \approx 10^4\mu$). As it is clear from equations (3.5) and (3.6), c_p is roughly 10^2 greater than c_s. Moreover, due to such distance between the 1st and 2nd Lamé coefficients, it is difficult to estimate both parameters at the same time. On the other hand, it is simple to decouple them, as it will be explored later in this work. The contribution to displacement given by compression waves becomes considerable at frequencies near 0 Hz, which are not involved in MRE experiments usually. Thus, the large wavelength of longitudinal waves does not allow for an effective estimation of λ [26].

3.2 Determination of mechanical parameters is an inverse problem

In an MRE experiment, the displacement is the quantity being measured through wave images as waves travel in the sample. Propagation of waves is described by an equation of motion, which represents the starting point to recover mechanical parameters. Indeed, knowing numerical values of displacement from a resting position and geometrical restrictions of the tissue, mechanical coefficients can be estimated inverting the equation of motion. For this reason, the mathematical problem consists in an inverse problem. Conversely, a direct problem would involve the calculation of stress and strain, already knowing the constitutive model and mechanical parameters of the material in exam.

In MRE, governing equations of motion are second order partial differential equations (PDE). Commonly, scalar Helmholtz inversion is the method allowing a solution to the inverse problem and, consequently, an estimation of the shear modulus from the wave equation [26]. In addition, other techniques including optimization algorithms are exploited to solve inverse problems. As an example, a study reports an algorithm consisting in calculating the minimum of an error function being the squared difference between the measured displacement and the displacement provided by a model [27].

The solution to the inverse problem in MRE is found under certain assumptions aiming at simplifying the physical context. If the medium can be considered elastic, isotropic and locally homogenous, there is no need to take boundary conditions and stress field into account when inverting the equation. Furthermore, as for most of the soft tissues the displacements detected are micrometric and consequent strains are under 1%, a further assumption about linearity can be made when dealing with the wave equation. The inversion technique will be further assessed in the following paragraphs.

3.3 Wave equation for an isotropic medium

To derive the wave equation, we begin from the equilibrium of body and surface forces in a continuum

$$\int_V \boldsymbol{F}\,dv + \int_S \boldsymbol{P}ds = 0 \qquad (3.8)$$

where $\boldsymbol{F}$ represents body forces and $\boldsymbol{P}$ surface forces. Referring to a cartesian coordinates system, equation (3.8) must hold for every direction. Applying divergence or Gauss law

$$\int_V (F_i + (\boldsymbol{\nabla} \cdot \boldsymbol{P})_i) dv = 0 \tag{3.9}$$

one can find the equation of motion inserting the definition of F given by Newton's second law:

$$\rho \frac{\partial^2 u_i}{\partial t^2} = \frac{\partial \sigma_{ij}}{\partial x_j} \tag{3.10}$$

with σ being the stress applied and x the position in space. Two basic assumptions are made: small deformations and absence of any strain if no stress is applied.

Stress and strain are related by the stiffness tensor C. For a linear, isotropic body it has only two independent parameters, λ and μ, as follows:

$$C = \begin{bmatrix} (2\mu+\lambda) & \lambda & \lambda & 0 & 0 & 0 \\ \lambda & (2\mu+\lambda) & \lambda & 0 & 0 & 0 \\ \lambda & \lambda & (2\mu+\lambda) & 0 & 0 & 0 \\ 0 & 0 & 0 & 2\mu & 0 & 0 \\ 0 & 0 & 0 & 0 & 2\mu & 0 \\ 0 & 0 & 0 & 0 & 0 & 2\mu \end{bmatrix} \tag{3.11}$$

with strain ε_{ij} and stress σ_{ij} being [25]

$$\varepsilon_{ij} = \begin{bmatrix} \varepsilon_{11} \\ \varepsilon_{22} \\ \varepsilon_{33} \\ \varepsilon_{23} \\ \varepsilon_{31} \\ \varepsilon_{12} \end{bmatrix} = \frac{1}{2}\left(\frac{\partial u_i}{\partial x_j} + \frac{\partial u_j}{\partial x_i}\right) \tag{3.12}$$

$$\sigma_{ij} = \begin{bmatrix} \sigma_{11} \\ \sigma_{22} \\ \sigma_{33} \\ \sigma_{23} \\ \sigma_{31} \\ \sigma_{12} \end{bmatrix} \tag{3.13}$$

In (3.11), λ and μ are real numbers for an elastic material and complex numbers if the medium is viscoelastic. Defining $\theta = tr[\varepsilon_{ij}] = \varepsilon_{ii} = \varepsilon_{11} + \varepsilon_{22} + \varepsilon_{33}$, and accounting for the stress-strain relation of isotropic, linear body

$$\sigma_{ij} = \lambda\theta\delta_{ij} + 2\mu\varepsilon_{ij} \tag{3.14}$$

where Kronecker delta $\delta_{ij} = 1$ for $i = j$ and $\delta_{ij} = 0$ for $i \neq j$, one can find the wave equation substituting (3.14) in (3.10) [25]:

$$\rho\frac{\partial^2 u_i}{\partial t^2} = \lambda\frac{\partial\theta}{\partial x_j} + 2\mu\frac{\partial\varepsilon_{ij}}{\partial x_j} \tag{3.15}$$

As stated previously, λ and μ are independent of position in a locally homogeneous sample. Last, inserting (3.12) in (3.15), the equilibrium as a function of displacement $\boldsymbol{u}$ is then determined:

$$\rho\frac{\partial^2 u_i}{\partial t^2} = \lambda\frac{\partial}{\partial x_i}\left(\frac{\partial u_1}{\partial x_1} + \frac{\partial u_2}{\partial x_2} + \frac{\partial u_3}{\partial x_3}\right) + \cdots$$

$$+\mu[\frac{\partial^2 u_i}{\partial x_1^2} + \frac{\partial^2 u_i}{\partial x_2^2} + \frac{\partial^2 u_i}{\partial x_3^2} + \frac{\partial}{\partial x_i}(\frac{\partial u_1}{\partial x_1} + \frac{\partial u_2}{\partial x_2} + \frac{\partial u_3}{\partial x_3})] \tag{3.16}$$

(3.16) is the extended form of vectoral equation (3.10).

3.3.1 Scalar Helmholtz equation for shear modulus recovery

As explained in paragraph 3.1, the parallel determination of both Lamé parameters is uncomfortable, due to the large difference λ and μ acquire in soft biological tissues. Nevertheless, decoupling such coefficients allows to focus on the research of μ only, being the most relevant in MRE.

λ needs to be neglected from equation of motion before performing the inversion to recover the shear modulus. Different methods have been exploited to disregard λ: applying a curl operator to the equation of motion, applying a high pass spatial filter since compression waves displacement is considerable at frequencies near 0 Hz, or simply mechanically exciting the tissue with harmonic shear motion. Also, accounting for incompressibility of the medium allows to neglect λ. An incompressible material is such if displacements caused by compression waves can be considered almost zero [28].

Before performing the inversion, it is useful to apply the Discrete Fourier Transform to the equation of motion (3.1), so that it results as follows

$$-\rho\omega^2\boldsymbol{U}(\omega) = (\lambda+\mu)\boldsymbol{\nabla}\big(\boldsymbol{\nabla}\cdot\boldsymbol{U}(\omega)\big) + \mu\Delta\boldsymbol{U}(\omega) \tag{3.17}$$

where $\boldsymbol{U}(\omega)$ is the DFT of displacement $\boldsymbol{u}$.

Moreover, the correspondence principle states that if the solution to the equation of motion for an elastic medium is available, then the solution in the frequency domain for a viscoelastic case can be expressed simply replacing elastic moduli with viscoelastic complex moduli [29]. In our notation, $\lambda(\omega)$ is the complex modulus of the 1st Lamé parameter, while $\mu(\omega)$ represents the complex modulus of the second Lamé coefficient. Accordingly, equation (3.17) becomes

$$-\rho\omega^2\boldsymbol{U}(\omega) = \big(\lambda(\omega)+\mu(\omega)\big)\boldsymbol{\nabla}\big(\boldsymbol{\nabla}\cdot\boldsymbol{U}(\omega)\big) + \mu(\omega)\Delta\boldsymbol{U}(\omega) \tag{3.18}$$

Considering now incompressibility of the sample, that holds

$$\boldsymbol{\nabla}\cdot\boldsymbol{U}(\omega) = 0 \tag{3.19}$$

equation (3.18) turns into the Scalar Helmholtz equation:

$$-\rho\omega^2\boldsymbol{U}(\omega) = \mu(\omega)\Delta\boldsymbol{U}(\omega) \tag{3.20}$$

Each component of the vector $\boldsymbol{U}$ satisfies the equation of motion thanks to the decoupling of terms in perpendicular directions. The determination of the Laplacian of $\boldsymbol{U}$ is the final step before inversion. The above equations are exploited in the direction the MEG is set along since it only encodes one direction per time. Last, the inversion can be performed to retrieve complex shear modulus:

$$\mu(\omega) = -\frac{\rho\omega^2 \boldsymbol{U}(\omega)}{\Delta \boldsymbol{U}(\omega)} \tag{3.21}$$

Such inversion procedure is used in two-dimensional elastography acquisitions assuming solely out-of-plane displacement, granted that data collected within a single slice are sufficient [30]. It returns an exact solution to the inverse problem, given some assumptions including isotropy and local homogeneity.

3.3.2 Algebraic Inversion of Differential Equations

In a three-dimensional MRE experiment, one can operate direct inversion exploiting a group algorithms called Algebraic Inversion of Differential Equations (AIDE) [26]. Two main approaches will be discussed in this chapter, both expressing the solution to the problem by means of a least square solution and considering local homogeneity: the application of the curl operator to the equation of motion and matrix direct inversion to determine viscoelastic moduli [31].

The first method consists in the application of a curl operator $\boldsymbol{Q} = \boldsymbol{\nabla} \times \boldsymbol{U}(\omega)$ to the wave equation (3.18). Since the divergence of a curl is equal to zero, the first term on the left-hand side of (3.18) vanishes:

$$\boldsymbol{\nabla} \cdot (\boldsymbol{\nabla} \times \boldsymbol{U}(\omega)) = \boldsymbol{\nabla} \cdot \boldsymbol{Q} = 0 \tag{3.22}$$

and the equation of motion is reduced to

$$-\rho\omega^2 \boldsymbol{Q} = \mu(\omega)\Delta \boldsymbol{Q} \tag{3.23}$$

The application of the curl allows to discard the contribution given by the compression wave. The inversion can be performed for each single pixel in an image, adopting the data from the neighboring pixels to calculate the derivatives [26]. The shear modulus is then yielded as follows:

$$\mu(\omega) = -\rho\omega^2 [(\Delta \boldsymbol{Q})^T (\Delta \boldsymbol{Q})]^{-1} (\Delta \boldsymbol{Q})^T \boldsymbol{Q} \tag{3.24}$$

Rewriting equation (3.18) so to separate $\mu(\omega)$ from $\lambda(\omega)$ terms as in (3.25), it is possible to develop a matrix A containing the spatial derivatives of displacement and multiplying the column vector $\boldsymbol{m}$ of the two unknowns $\mu(\omega)$ and $\lambda(\omega)$ (equation (3.26)).

$$-\rho\omega^2\boldsymbol{U}(\omega) = \mu(\omega)\{\Delta\boldsymbol{U}(\omega) + \boldsymbol{\nabla}(\boldsymbol{\nabla}\cdot\boldsymbol{U}(\omega))\} + \lambda(\omega)\boldsymbol{\nabla}(\boldsymbol{\nabla}\cdot\boldsymbol{U}(\omega)) \tag{3.25}$$

$$-\rho\omega^2\begin{bmatrix}U_1(\omega)\\U_2(\omega)\\U_3(\omega)\end{bmatrix} = A\begin{bmatrix}\mu(\omega)\\\lambda(\omega)\end{bmatrix} \tag{3.26}$$

Consequently, A acquires the form:

$$A = \begin{bmatrix}\Delta U_1(\omega) + \dfrac{\partial(\boldsymbol{\nabla}\cdot\boldsymbol{U}(\omega)}{\partial x_1} & \dfrac{\partial(\boldsymbol{\nabla}\cdot\boldsymbol{U}(\omega))}{\partial x_1}\\ \Delta U_2(\omega) + \dfrac{\partial(\boldsymbol{\nabla}\cdot\boldsymbol{U}(\omega))}{\partial x_2} & \dfrac{\partial(\boldsymbol{\nabla}\cdot\boldsymbol{U}(\omega))}{\partial x_2}\\ \Delta U_3(\omega) + \dfrac{\partial(\boldsymbol{\nabla}\cdot\boldsymbol{U}(\omega))}{\partial x_3} & \dfrac{\partial(\boldsymbol{\nabla}\cdot\boldsymbol{U}(\omega))}{\partial x_3}\end{bmatrix} \tag{3.27}$$

It is evident from equation (3.26) that the problem is overdetermined. Indeed, the column vector of the unknown model parameters $\boldsymbol{m}(\omega) = \begin{bmatrix}\mu(\omega)\\\lambda(\omega)\end{bmatrix}$ has only two components, while the column vector of displacement data $\boldsymbol{U}(\omega) = \begin{bmatrix}U_1(\omega)\\U_2(\omega)\\U_3(\omega)\end{bmatrix}$ has got three terms. A linear solution to such system can be found by means of a least square approximation, consisting in minimizing the sum of the square of the error given by the discrepancy between measured and model displacements [32].

Defining

$$\varepsilon_i(\omega) = U_i(\omega) - \sum_{j=1}^{2} A_{ij}m_j(\omega) \tag{3.28}$$

$$E(\omega) = \sum_{i=1}^{3} (\varepsilon_i(\omega))^2 \tag{3.29}$$

The minimum of the error ε can be found nulling its derivative with respect to the two components of vector $\boldsymbol{m}$:

$$\frac{\partial \varepsilon(\omega)}{\partial m_k(\omega)} = 2 \sum_{i=1}^{3} \left(U_i(\omega) - \sum_{j=1}^{2} A_{ij} m_j(\omega) \right) \left(-A_{ij} \right) = 0 \tag{3.30}$$

being $k = 1{,}2$. Equation (3.30) holds that

$$\sum_{j=1}^{2} \left(\sum_{i=1}^{3} A_{ij} A_{ik} \right) m_j(\omega) = \sum_{i=1}^{3} U_i(\omega) A_{ik} \tag{3.31}$$

From (3.31), one can notice that if

$$A^T A \boldsymbol{m}(\omega) = A^T \boldsymbol{U}(\omega) \tag{3.32}$$

the solution $\boldsymbol{m}$ will be

$$\boldsymbol{m}(\omega) = (A^T A)^{-1} A^T \boldsymbol{U}(\omega) \tag{3.33}$$

Therefore:

$$\begin{bmatrix} \mu(\omega) \\ \lambda(\omega) \end{bmatrix} = (A^T A)^{-1} A^T \begin{bmatrix} U_1(\omega) \\ U_2(\omega) \\ U_3(\omega) \end{bmatrix} \tag{3.34}$$

Differently from the application of the curl operator, the latter algorithm does not discard the 1st Lamé coefficient $\lambda(\omega)$, thus considering also the contribution to displacement provided by compression waves in the medium.

3.3.3 Equation of motion and shear modulus recovery for a transversely isotropic viscoelastic medium

Human skeletal muscle cannot be considered as an isotropic medium. Indeed, it has got a peculiar geometric distribution of parallel fibers, constituting the basic repetitive unit of the muscular tissue [33]. Within each fiber, myofibrils are disposed in series; by themselves, myofibrils are composed of sarcomeres disposed in series, able to actively develop force thanks to adenine and myosin contractile proteins [34]. Such structure generates a preferential direction for the propagation of waves parallel to fibers. Therefore, when assessing wave propagation in skeletal muscles, the medium should be regarded as anisotropic.

In the following section, viscoelasticity is addressed being the muscle a soft tissue, thus making an analysis across a range of mechanical vibration frequencies necessary to consider damping of waves. Linear constitutive equations can be adopted in the environment of MRE, since small displacements and deformations are considered. As previously stated, the amplitude of mechanical excitation provided to the tissue is about in the order of tens on microns.

Due to its fibrous composition with parallel and serially-disposed fibers, the skeletal muscle can be represented as a transversely isotropic material [35]. In the skeletal muscle case, transverse isotropy involves one main direction for mechanical behavior, parallel to fibers. The symmetry axis is then parallel to fibers and it defines the planes of symmetry of the model [36]. The plane of isotropy is orthogonal to the direction of fibers: muscular properties do not vary with direction within such plane (Figure 7).

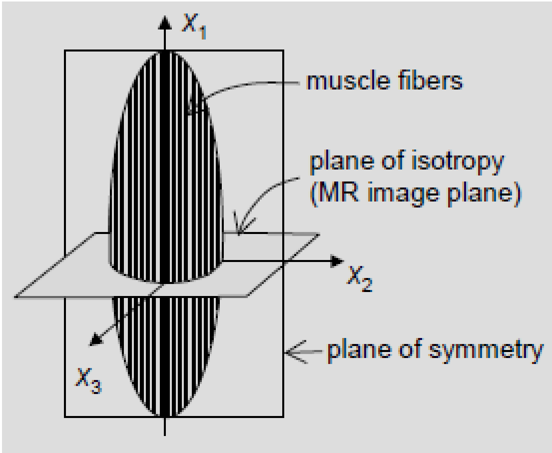

Figure 7: Transversely isotropic model for human skeletal muscle. X_1 coincides with symmetry axis and defines infinite planes of symmetry. The plane of isotropy is identified by X_2 and X_3 directions: tissue properties do not vary depending on direction on such plane. Provided by Prof. Klatt.

The adoption of a transverse isotropic model decreases the number of independent elastic parameters to five in the stress-strain relations: two Young's moduli, a single shear modulus and a couple of Poisson's ratios. Compliance tensor (relating stress to strain) will then acquire the following form:

$$\begin{bmatrix} \varepsilon_1 \\ \varepsilon_2 \\ \varepsilon_3 \\ \varepsilon_4 \\ \varepsilon_5 \\ \varepsilon_6 \end{bmatrix} = \begin{bmatrix} \frac{1}{E_1} & -\frac{\gamma_{21}}{E_2} & -\frac{\gamma_{21}}{E_2} & 0 & 0 & 0 \\ -\frac{\gamma_{12}}{E_1} & \frac{1}{E_2} & -\frac{\gamma_{32}}{E_2} & 0 & 0 & 0 \\ -\frac{\gamma_{12}}{E_1} & -\frac{\gamma_{23}}{E_2} & \frac{1}{E_2} & 0 & 0 & 0 \\ 0 & 0 & 0 & 2\frac{1+\gamma_{23}}{E_2} & 0 & 0 \\ 0 & 0 & 0 & 0 & \frac{1}{\mu_{12}} & 0 \\ 0 & 0 & 0 & 0 & 0 & \frac{1}{\mu_{12}} \end{bmatrix} \begin{bmatrix} \sigma_1 \\ \sigma_2 \\ \sigma_3 \\ \sigma_4 \\ \sigma_5 \\ \sigma_6 \end{bmatrix} \tag{3.35}$$

Assuming incompressibility for soft biological tissues [35] due to high presence of water, those parameters further reduce to three: a ratio between parallel and normal to fibers Young's moduli and two shear moduli [37].

Moreover, since soft tissues noticeably damp the amplitude of the propagating waves, resulting in the necessity of considering viscoelastic properties instead of elastic ones. To find viscoelastic properties, it would be possible to apply the correspondence principle as stated previously: known the solution to the equation of motion for an elastic medium, the solution for a linear viscoelastic system would only require to insert frequency-dependent viscoelastic parameters in wave equation (3.10). Another way to determine the solution would involve the substitution of the stress-strain relation for the anisotropic case into the equation of motion. Thus, complex shear stiffness can be divided into a real and an imaginary part in frequency domain as follows:

$$\mu(\omega) = \mu_{Re} + j\mu_{Im} \tag{3.36}$$

where j is the imaginary unit. μ_{Im} represents the damping term or loss modulus of the viscoelastic model, while μ_{Re} coincides with the storage modulus [38]. Then, for a viscoelastic medium, one can identify the stress-strain relationship through two distinct fourth-order tensors C and D, one consisting of stiffness terms and the other containing damping components, respectively.

$$\sigma_{ij}(\omega) = C\varepsilon_{kl}(\omega) + D\frac{\partial\varepsilon_{kl}(\omega)}{\partial t} \tag{3.37}$$

The two matrices will have a common composition:

$$C; D = \begin{bmatrix} (2\mu_\perp + \lambda_\perp) & \lambda_M & \lambda_M & 0 & 0 & 0 \\ \lambda_\perp & (2\mu_\perp + \lambda_\perp) & \lambda_\perp & 0 & 0 & 0 \\ \lambda_M & \lambda_M & (2\mu_\parallel + \lambda_\parallel) & 0 & 0 & 0 \\ 0 & 0 & 0 & 2\mu_\parallel & 0 & 0 \\ 0 & 0 & 0 & 0 & 2\mu_\parallel & 0 \\ 0 & 0 & 0 & 0 & 0 & 2\mu_\perp \end{bmatrix} \tag{3.38}$$

being $\mu_\parallel, \mu_\perp, \lambda_\parallel, \lambda_\perp$ the 1st and 2nd Lamé coefficients in the parallel and normal to fibers direction, respectively. λ_M is the compressive strength of the material, including both $\lambda_\parallel$ and $\lambda_\perp$. In the stiffness tensor, the components are the real parts of the Lamé parameters, whereas the damping tensor contains their imaginary terms.

Finding mechanical parameters of interest from the equation of motion in an MRE experiment requires further simplifications coinciding with the adoption of the transverse isotropic model to reduce the number of unknows with respect to the equations available. In a homogeneous, linear, viscoelastic and anisotropic medium tensors C and D are symmetric and include only five independent components. Those terms are $\mu_\parallel, \mu_\perp, \lambda_\parallel, \lambda_\perp$ and λ_M; furthermore, the number of independent parameters could be further reduced to three, since in biological tissues only a single longitudinal and two shear waves propagate relevantly, being $\lambda_\parallel = \lambda_\perp = \lambda_M = \lambda$.

Hence, substituting equation (3.37) in (3.10)

$$\rho \frac{\partial^2 u_i}{\partial t^2} = \frac{\partial \left(C\varepsilon_{kl}(\omega) + D \frac{\partial \varepsilon_{kl}(\omega)}{\partial t} \right)}{\partial x_j} \tag{3.39}$$

and knowing strain-displacement relation (3.12), the equation of motion for a transversely isotropic, homogeneous and linear medium is:

$$\rho \frac{\partial^2 u_i}{\partial t^2} = C_{ijkl} \frac{\partial^2 u_l}{\partial x_j \partial x_k} + D_{ijkl} \frac{\partial^3 u_l}{\partial t \partial x_j \partial x_k} \tag{3.40}$$

Identifying $\tau = \mu_\parallel - \mu_\perp$, and accounting for incompressibility, the equation of motion is rewritten as follows:

$$\rho \frac{\partial^2 u_i}{\partial t^2} = \mu_\perp u_{i,jj} + \tau \begin{bmatrix} \frac{\partial^2 u_1}{\partial x_3^2} + \frac{\partial^2 u_3}{\partial x_1 \partial x_3} \\ \frac{\partial^2 u_2}{\partial x_3^2} + \frac{\partial^2 u_3}{\partial x_2 \partial x_3} \\ \frac{\partial^2 u_3}{\partial x_1 \partial x_2} \end{bmatrix} + \eta \frac{\partial u_{i,jj}}{\partial t} \tag{3.41}$$

Finally, transforming in frequency domain and applying curl to (3.41) allows to obtain the scalar Helmholtz equation, with contributions related only to propagation of shear waves. It is possible then to recover the shear parameters object of this experiment.

$$-\rho\omega^2 q_i = \mu_\perp q_{i,jj} + \tau \begin{bmatrix} \frac{\partial^3 u_1}{\partial x_3^3} - \frac{\partial^3 u_3}{\partial x_1 \partial x_2^2} - \frac{\partial^3 u_3}{\partial x_1^3} \\ \frac{\partial^2 u_3}{\partial x_1^2 \partial x_2} + \frac{\partial^2 u_3}{\partial x_2 \partial x_3} - \frac{\partial^3 u_2}{\partial x_3^3} \\ \frac{\partial^2 u_3}{\partial x_1 \partial x_2} \end{bmatrix} + i\omega\eta q_{i,jj} \quad (3.42)$$

with $q_i = \varepsilon_{ijk} \frac{\partial u_k}{\partial x_j}$. An algorithm optimizing the determination of the shear stiffness can be used; multiple references such as [26] and [27] can be addressed to further explore it.

3.4 Direct problem

Alternatively to the inverse problem approach, the direct problem aims at finding the displacement field having as input the viscoelastic properties of the test material. Therefore, the direct problem allows to analyze wave propagation within the sample, assuming knowledge about the aforementioned properties. In MRE computational simulations, a direct problem is assessed as the phantom mechanical properties are given in input to the model. In this study, COMSOL Multiphysics 5.3a is exploited to set a direct problem with the goal to obtain wave images over different excitation frequencies, being the viscoelastic properties of the tested phantom model already known.

CHAPTER 4

STATE-OF-THE-ART

As only little in literature has been discussed about the effects axial pre-strain boundary conditions might have on the propagation of shear waves within a skeletal muscle-like phantom, the principal purpose of the present work is to investigate how variations in the shear modulus of the material composing the phantom generated by axial elongation could influence the diffusion of vibration. Indeed, the consequences of longitudinal pre-stretching of the specimen should reflect in a change in the inner structure of the material, affecting the shear stiffness derivable through MRE [39]. The analysis of the repercussions of passive loading of a skeletal muscle might help in understanding how passive tensile reaction plays a role in tissue stiffening.

4.1 Ecoflex™ phantom

Due to its excellent soft tissue mimicking features, durability and stability in time, Ecoflex™ is suitable for a simulation of propagation of waves in a soft tissue-like sample geometry. Ecoflex™ does not suffer from relaxation phenomena while loaded for the typical duration of an MRE scan [39][40]. Therefore, it is well suited for an analysis involving at the same time axial pre-strain and mechanical shear excitation during MRE acquisition.

A study from Spencer and Klatt investigates the effect of axial pre-strain on a homogeneous Ecoflex™ 0010 cylindrical phantom, in terms of MRE-determined complex shear modulus. Real and imaginary shear moduli, analyzed separately, both linearly rise with increasing excitation frequency, as demonstrated also by Klatt et al. in 2010 [41]. The real part of the shear modulus, also, increases with the magnitude of axial pre-straining. Such phenomenon is visible, at first sight, with stretching wavelength of the propagating shear waves [39], and it is confirmed also by the existing direct proportionality between shear modulus and wavelength, as stated in equation (4.1)

$$\lambda = \frac{1}{f}\sqrt{\frac{|\mu|}{\rho}} \qquad (4.1)$$

4.2 Viscoelastic models for biological soft tissues

As a direct approach is needed when addressing computational simulations of MRE experiments, viscoelastic models are required to represent the complex behavior of shear modulus depending on stimulation frequency. In such case, material properties are known already, and they are fit into a viscoelastic model relating stress and strain within the sample. The fibrous architecture of a skeletal muscle would suggest the adoption of a power law to model the viscoelastic structure of the tissue. In such a context, the shear modulus would be proportional to the mechanical excitation angular frequency ω to the power of α [41]. A few studies have confirmed the suitability of a two- or three-parameter power law model to represent the viscoelastic properties of biological soft tissues, such as brain [2][42] and skeletal muscle [43]. Specifically, soft tissues could be well modeled by a power law involving $\alpha < 0.5$. The validity of the power law is supported by an *in vivo* MRE study on skeletal muscle, which found that the rate between imaginary and real parts of complex shear modulus remains constant with increasing vibration frequency [41]. Among fibrous *in vivo* tissues, liver and skeletal muscle are both well modeled through the Spring-Pot model [2][41].

4.2.1 Fractional Voigt Model

Amidst parametric viscoelastic models, Fractional Voigt is a three-parameter model including a power law and a stationary term. It is an effective model to represent the dynamic mutation of the shear modulus of Ecoflex™, as it is formed by a Spring-Pot (defined by two parameters α and μ_α) and a static shear modulus μ_0, placed in parallel (Figure 8).

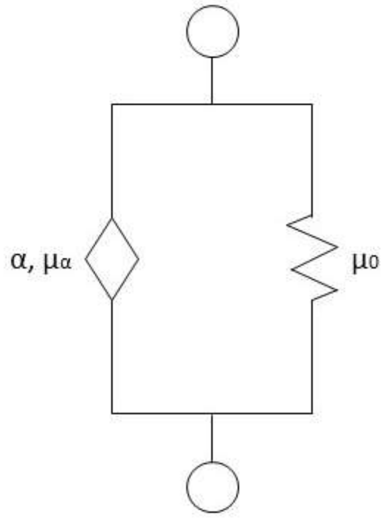

Figure 8: The Fractional Voigt model, with a Spring-Pot and a spring in parallel. The three parameters characterizing such model are visible: α and μ_α representing the Spring-Pot, and μ_0 for the spring.

Indeed, the spring allows the entire model to stand a static load, while the Spring-Pot portion has excitation velocity dependent shear deformation, as in (4.2).

$$\mu = \mu_0 + \mu_\alpha \frac{\partial^\alpha}{\partial t^\alpha} \tag{4.2}$$

being $0 < \alpha < 1$.

When addressing MRE experimental studies with Ecoflex™, Fractional Voigt model involves a little estimation error (3.8%) with respect to other parametric models, e.g. Spring-Pot alone, being the estimation error the normalized difference between the shear modulus calculated through the model and the shear modulus obtained through experimental MRE [40].

In the Fractional Voigt model, real and imaginary parts of the complex shear modulus assume the expressions (4.3) and (4.4), respectively.

$$\mu_{Re} = \mu_0 + \mu_\alpha \omega^\alpha \cos\left(\alpha \frac{\pi}{2}\right) \tag{4.3}$$

$$\mu_{Im} = \mu_\alpha \omega^\alpha \sin(\alpha \frac{\pi}{2}) \qquad (4.4)$$

The complex shear modulus is defined as in equation (4.5), where *i* is the imaginary unit ($i = \sqrt{-1}$):

$$\mu = \mu_{Re} + i\mu_{Im} \qquad (4.5)$$

CHAPTER 5

MATERIALS AND METHODS

5.1 Transversely isotropic phantom preparation

The phantom has a cylindrical shape with enlarged ends (Figure 9) to best suit the constraints given by both diameter of magnetic coil (Agilent 9.4T, 72 mm ID size Radiofrequency (RF) coil, 205/120 HD, 300mA, 600mT/m, Agilent Technologies Inc., Santa Clara, CA, USA) and the necessity to be held still at a precise axial elongation during each scan.

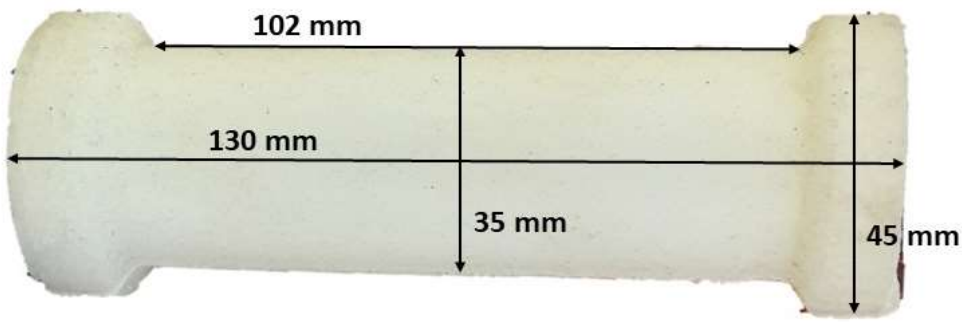

Figure 9: Ecoflex^{TM} phantom longitudinal view. Two enlarged cylindrical ends of 45 mm in diameter ensure the possibility to hold the sample fixed at a desired axial deformation value with two couples of clamps, as explained in paragraph 6.2.2.

Five smaller cylinders are embedded into one larger cylinder to simulate the presence of fibers. A sketch of the cross section of the phantom is visible in Figure 10, coinciding with the plane of isotropy in the transverse isotropy model. The fibers are disposed axisymmetrically and have equal length to phantom, so to guarantee they run across the ROI. The phantom is made of Ecoflex^{TM} (Smooth-On, Inc., Macungie, PA, USA), a skin-safe silicone rubber that can be cured at room temperature with negligible shrinkage. The material guarantees a response to load close to soft biological tissues [44] and its stiffness, to be determined through MRE, increases with mechanical stimulation frequency. It can be easily scanned with H^1 Magnetic Resonance Imaging [13] [41].

In addition, Ecoflex^{TM} suffers less mechanical properties change in time with respect to gelatin based phantoms, common in Magnetic Resonance Elastography analyses [45].

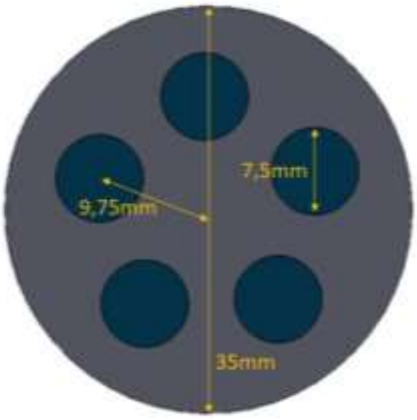

Figure 10: Cross sectional view of the Ecoflex^{TM} transversely isotropic phantom. In dark blue, the five small cylinders made of Ecoflex^{TM} 0030 are disposed axisymmetrically and simulate biological fibers in a skeletal muscle. The surrounding matrix is made of Ecoflex^{TM} 0010, lower in tensile strength with respect to fibers' Ecoflex^{TM} 0030.

A hollow 3D printed cylindrical mold with cylindrical enlarged ends is used to give the Ecoflex^{TM} the shape visible in Figure 9. Five cylindrical columns disposed axisymmetrically in the larger concave cylinder and attached to a cylindrical base, which is fixed at one of the two ends of the hollow cylinder, allow to leave space for the creation of the fibers.

First, liquid Ecoflex^{TM} 0010 is poured into the concave structure above descripted keeping a uniform flow to minimize entrapped air, to form the external connective tissue matrix-resembling part of the phantom. It is then cured at room temperatures for 24 hours. The entire mold is then manually removed, including the five cylindrical columns that leave in this way room to pour Ecoflex^{TM} 0030 constituting the fibers. Identically, Ecoflex^{TM} 0030 is left curing for 24 hours.

5.2 Mechanical setup design and fabrication

The setup is first conceptualized and designed on SolidWorks software (Dassault Systèmes, Vélizy-Villacoublay, France). Every component is designed singularly, knowing that the whole setup must satisfy the dimensional constraints imposed by the 72 mm ID of the RF coil and the

1206 mm length of the magnetic bore (Agilent 9.4T). The aim of the setup is to provide support to hold the phantom still while mechanically excited through shear deformation of 11.6 μm amplitude at different frequencies by a P-840.10 piezoelectric driver model (Physik Instrumente, Karlsruhe, Germany) during an MR scan. A brief overview on each component and on the setup in its whole is given in the following paragraphs. Every component is 3D printed or manually shaped at University of Illinois at Chicago Makerspace, 728 W Roosevelt Road, 60607, Chicago.

5.2.1 Holding tube

The whole setup is held by a half-tube, cut parallelly to its longitudinal axis 3 mm below the horizontal diameter defining the half of its cross section. The half-pipe is cut from a clear cast acrylic tube (McMaster-Carr Supply Company, Elmhurst, IL, USA). The Outer Diameter (OD) of the tube is 70 mm, leaving 1 + 1 mm spacing between the magnet and tube surfaces. Internal Diameter (ID) is 56 mm, so to have room to fit every component in. The length of the half-pipe is 700 mm. At one end of the tube a 506 mm long rod is screwed to the cross-sectional surface of the pipe, to reach the 1206 mm length of the bore. In this way, the setup allows to keep the phantom inside ROI of the coil at the beginning of each scan, after having taken the whole setup out of the bore to adjust the length of the phantom. On the borders of the tube, a series of drilled holes is designed to fix two couples of clamps, which will be illustrated further on in this chapter.

5.2.2 Clamps

To hold the cylindrical phantom elongated while running the scan, two couples of semicircular clamps are used (Figure 11). The ID of such clamps matches the ID of the phantom: clamping the sample just before its enlarged ends, it is guaranteed that the phantom does not shrink to its resting position. Every clamp is 3D printed in VeroClear acrylic photopolymer (Stratasys Ltd, Eden Prairie, MN, USA).

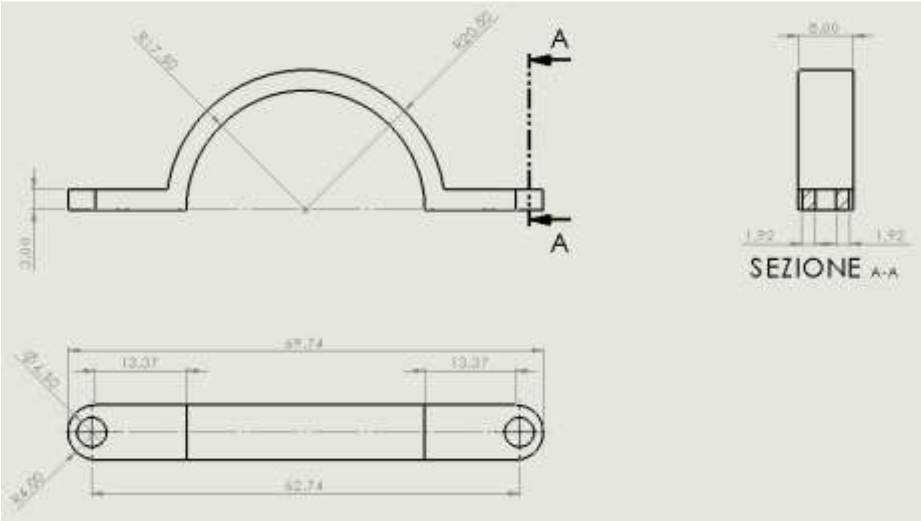

Figure 11: The semicircular clamps holding the phantom still while elongated. A few copies of the clamps, with decreasing ID as the sample ID reduces with applied longitudinal stress, are provided. All dimensions are in mm. Image made with SolidWorks.

5.2.3 Excitation rings

To transform longitudinal motion provided by PI piezo actuator into shear motion applied to the phantom, VeroClear 3D printed rings are used. For each strain level of the phantom, ID of each ring is .4 mm shorter than sample ID to ensure a uniform gripping pressure on the surface of the phantom (TABLE I). Indeed, to create a contact surface between ring and phantom, the silicone cylinder is inserted in the ring. Each ring has a 15 mm thickness and it is traversed by 4 equally spaced clearance holes to connect the ring to the rest of the structure providing mechanical vibration (Figure 12).

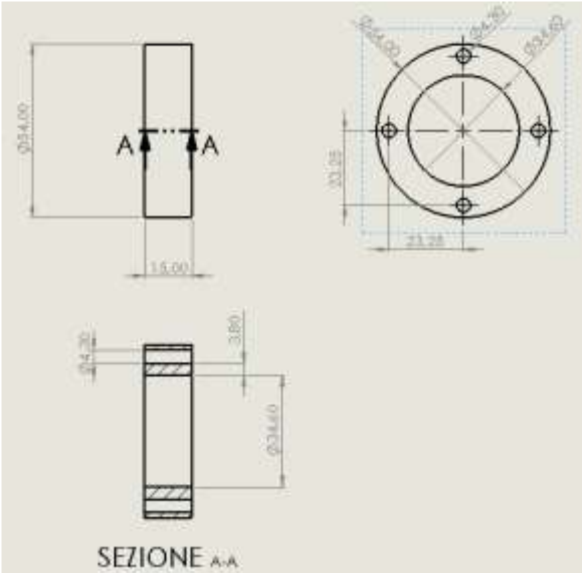

Figure 12: Ring providing homogeneous shear excitation to phantom. The four holes allow to screw the ring to the rest of the vibratory structure. All dimensions are in mm. Image made with SolidWorks.

TABLE I: CORRELATION BETWEEN PHANTOM DIMENSIONS AT EVERY SPECIFIC STRAIN LEVEL. LAST COLUMN SHOWS THE ID OF THE VIBRATION RING, 0.4 MM SHORTER THAN THE ACTUAL DIAMETER OF THE PHANTOM TO ASSURE HOMOGENEOUS GRIP PRESSURE AT PHANTOM SURFACE.

Length [mm]	Longitudinal strain %	Diameter [mm]	Lateral strain %	ID of ring [mm]
102	0	35	0	34,6
122,4	20	31,5	-9,95	31,1
142,8	40	28	-19,91	27,6
163,2	60	24,5	-29,86	24,1
183,6	80	21	-39,82	20,6
204	100	17,5	-49,77	17,1

5.2.4 Legs and base

Four legs and an X-shaped parallelogram base are screwed together, connecting a rod moved by the piezo actuator to the mentioned shear ring. All those pieces are VeroClear 3D printed. The screws are made of nylon, so to be suitable with MR imaging requisites. The parallelogram has four clearance holes at the same radial position to that of ring's holes, which is 23.25 mm away from the longitudinal axis (Figure 13). The legs are then screwed at one end to such parallelogram, and at the other end to the excitation ring (Figure 17).

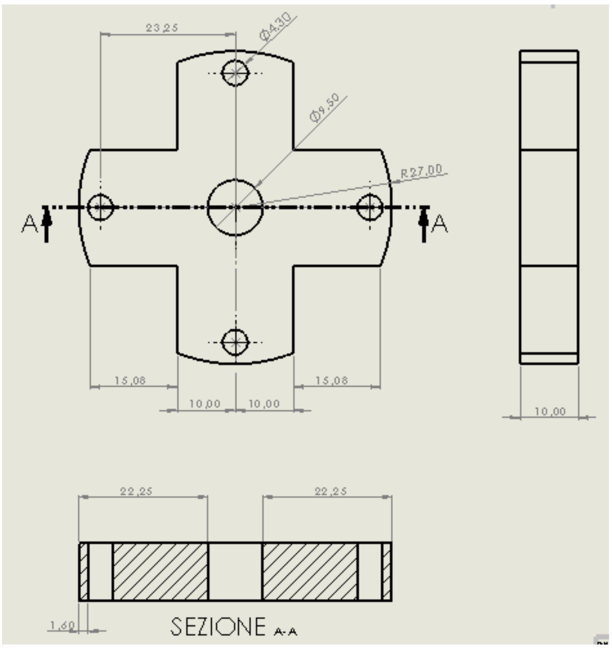

Figure 13: X-shaped base parallelogram with the central drilled hole to screw the connecting rod in and the four clearance holes to fix the legs. They are screwed to the excitation ring at their other end. All dimensions are in mm. Image made with SolidWorks.

5.2.5 <u>Rod</u>

A nylon rod connects the legs-parallelogram structure to the piezoelectric actuator. The rod is secured to the parallelogram by a couple of bolts and screwed to the piezo by a smaller threaded rod (Figure 14).

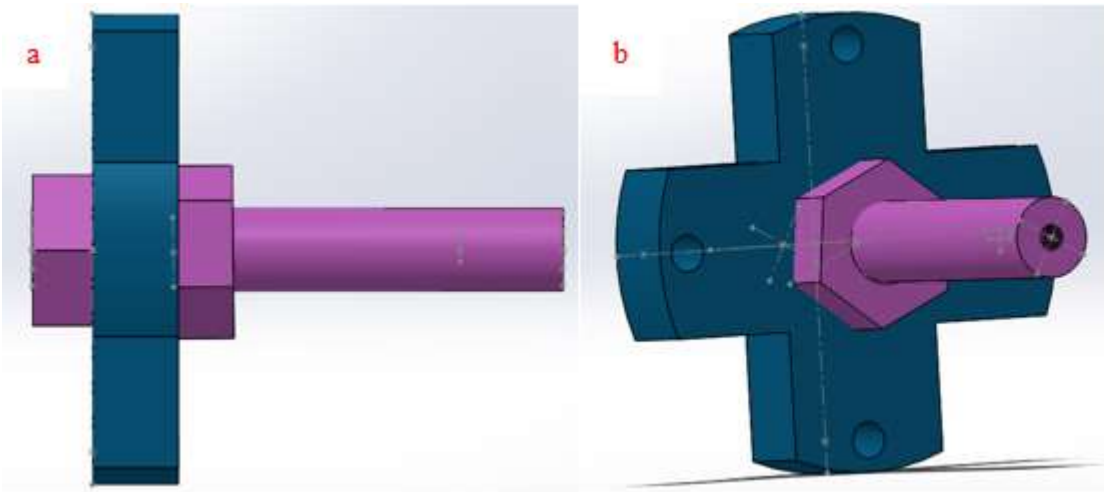

Figure 14: a) Coupling of the rod to X-shaped base through a couple of bolts. b) clearance holes are visible at the extremities of the parallelogram. Made with SolidWorks.

5.2.6 L-shaped piece and rail

The piezo actuator is kept in position by an L-shaped VeroClear 3D printed component, that can be screwed to a hemicylindrical rail, also VeroClear 3D printed. The rail OD coincides with the ID of the holder tube. The rail has a series of threaded holes to fix the L-shaped piece and another series of clearance holes to allow fixing of the rail itself to the supporting tube (Figure 15).

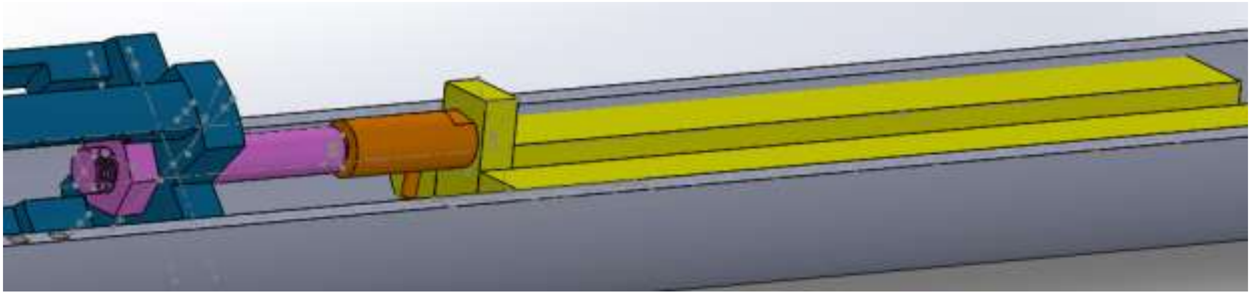

Figure 15: Zoom on the three-dimensional design of the setup portion holding the piezoelectric actuator (in orange). Such section includes the hemicylindrical rail and the L-shaped component, both depicted in yellow. The longitudinal motion generated by the piezo is transmitted to the rod, which is fixed to the parallelogram-and-legs structure through a couple of nuts (only one visible from this perspective). Made with SolidWorks.

5.3 Preliminary testing

The effectiveness of the setup is assessed through a couple of preliminary tests. The common aim of both tests is to understand whether the longitudinal motion is properly transmitted from P.I. piezoelectric actuator all the way to the excitation ring.

5.3.1 Vibration exciter

Response to vibratory input stimulus is first tested with Brüel & Kjær Vibration Exciter Type 4089 (Brüel & Kjær, Denmark). The key components of the setup for the transmission of the movement (i.e. piezo – used only as a connector in the present test – rod, X-shaped base, legs and excitation ring) are vertically connected to the exciter (Figure 16). Two accelerometers (PCB Piezotronics, Depew, NY, USA) are glued at the top of the setup, at the cross section of the excitation ring. Another accelerometer connecting the exciter to the setup allow to compare the motion provided by the shaker to the effective displacement of the ring at the top of the setup. The transfer function of the displacement of the setup (amplitude of the displacement at the top divided by the amplitude of the displacement at the bottom) is displayed on Agilent 35670A Dynamic Signal Analyzer (Agilent Technologies Inc., Santa Clara, CA, USA). Mechanical excitation frequency is 500 Hz.

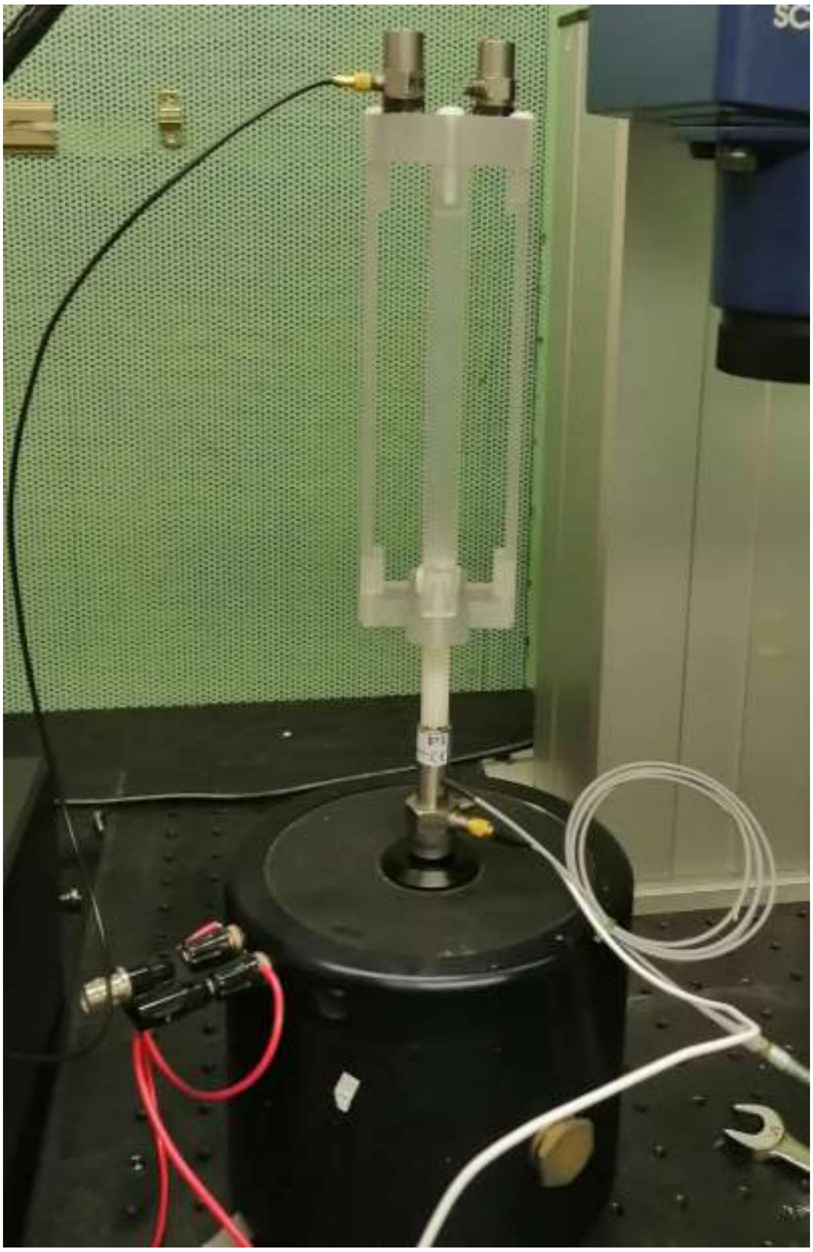

Figure 16: Setup testing with Brüel & Kjær Vibration Exciter Type 4089. The setup is vertically connected through an accelerometer to the mechanical exciter. Another accelerometer on top of the ring allows to show the displacement on Agilent 35670A Dynamic Signal Analyzer.

5.3.2 Single Point Laser Doppler Vibrometry

The second test to assess the effective transmission of longitudinal motion from the piezo includes a Polytec Portable Digital Vibrometer (PDV) 100 (Polytec GmbH, Waldbronn, Germany). An Agilent E3631A Triple Output DC Power Supply connected to an Agilent 33210A 10 MHz Function / Arbitrary Waveform Generator activate the piezoelectric driver with a voltage through a Yamaha P7000S power amplifier. In parallel to the amplifier – piezo connection, a Tektronix TDS210 Two Channels Oscilloscope (Tektronix Inc., Beaverton, OR, USA) is linked to the power amplifier. The PDV is connected to the oscilloscope, so that the latter can show both the input and output signals (to the piezo actuator the former, from the PDV the latter).

5.4 MRE in Agilent 9.4T coil

The MRE acquisition is taken at a single shear excitation frequency with the Agilent 9.4T magnetic coil. The ID of the RF coil is 72 mm, as previously specified. A Spin Echo RF pulse is used, characterized by TE = 0.02162 s and TR = 1.0 s, obtaining proton density image. Field of View (FOV) is 4.8 x 4.8 cm and image dimensions are 64 x 64 pixels. Slice thickness is set at 1 mm, and 10 slices are acquired within the ROI. The periodic mechanical vibration frequency provided by P-840.10 piezo is set at 500 Hz. The amplitude of such displacement equals 11.6 μm.

5.5 MRE computational simulations

To investigate how the Ecoflex™ phantom might behave under longitudinal prestrain conditions applying a harmonic shear vibration, MRE finite element simulations are conducted using COMSOL Multiphysics® 5.3a (Stockholm, Sweden). The phantom is built on SolidWorks, simplifying its geometry to a cylinder 35 mm in diameter and 100 mm in height, and imported into COMSOL Multiphysics® 5.3a. It includes the five fibers as well, positioned axisymmetrically at 9.75 mm from the axis and having 7.5 mm diameter, as depicted in the snapshots in TABLE III.

Once the geometry is imported into COMSOL Multiphysics® 5.3, material properties are assigned to the different domains, as specified in TABLE II. The domains include the external matrix and the five fibers. As the computational experimentation requires a direct problem approach, the relevant mechanical properties of Ecoflex™ are given as input parameters to the simulation, including the complex shear modulus, defined through the Fractional Voigt viscoelasticity model [40]. Density of Ecoflex™ is similar to that of water (1000 kg/m^3).

TABLE II: INPUT PARAMETERS INSERTED INTO COMSOL MULTIPHYSICS 5.3a FOR MRE COMPUTATIONAL SIMULATION. *i* REPRESENTS THE IMAGINARY UNIT.

Description (symbol)	Value	Formula
Poisson's ratio (ν)	0.499998	
Density (ρ)	1000 kg/m^3	
Frequency (f)	500 Hz	
First Fractional Voigt model parameter (μ_α)	1.956 Pa	
Second Fractional Voigt model parameter (α)	0.34	
Tensile strength Ecoflex™ 0010 (μ_{0_10})	827371 Pa	
Tensile strength Ecoflex™ 0030 (μ_{0_30})	1.379E6 Pa	
Young's modulus Ecoflex™ 0010 (E_{10})	36890 Pa	
Young's modulus Ecoflex™ 0030 (E_{30})	68948 Pa	
Real shear modulus Ecoflex™ 0010 (μ_{Re_10})	8.274E5 Pa	$\mu_{0\_10} + \mu_\alpha*2\pi f*\cos(\alpha\pi/2)$
Real shear modulus Ecoflex™ 0030 (μ_{Re_30})	1.379E6 Pa	$\mu_{0\_30} + \mu_\alpha*2\pi f*\cos(\alpha\pi/2)$
Imaginary shear modulus Ecoflex™ 0010 (μ_{Im_10})	15.387 Pa	$\mu_\alpha*2\pi f*\sin(\alpha\pi/2)$

Imaginary shear modulus Ecoflex™ 0030 (μ_{Im_30})	15.387 Pa	μ_α*2πf*sin(απ/2)
Complex shear modulus Ecoflex™ 0010 (μ_{10})	(8.274E5+*i**15.387) Pa	$\mu_{Re\_10} + i\mu_{Im\_10}$
Complex shear modulus Ecoflex™ 0030 (μ_{30})	(1.379E6+*i**15.387) Pa	$\mu_{Re\_30} + i\mu_{Im\_30}$
Bulk modulus Ecoflex™ 0010 (K_{10})	(2.0865E11+*i**3.8467E6) Pa	(2*μ_{10})(1+ν) / (3-6 ν)
Bulk modulus Ecoflex™ 0030 (K_{30})	(3.4476E11+*i**3.8467E6) Pa	(2*μ_{30})(1+ν) / (3-6 ν)

The mesh selected for the simulation varies with the frequency of the harmonic shear excitation. The trade-off between detailed views of wave propagation and computational time conduces to the use of COMSOL Multiphysics® 5.3a pre-set *Normal* element size mesh for frequencies up to 2500 Hz, while *Finer* element size one for the range of frequencies including 3000 Hz, 3500 Hz and 4000 Hz. TABLE III shows an axial cross-sectional view of both meshes and details about the triangular elements constituting the meshes.

Axial pre-strained boundary conditions are applied through four different values of the ε_{zz} component of the strain tensor, namely 0%, 10%, 20% and 50% of the length at rest of the phantom model. Thus, a total of 32 simulations are run – eight frequencies for each pre-strain value.

TABLE III: TOP ROW: AXIAL CROSS-SECTIONAL REPRESENTATION OF PHANTOM GEOMETRY AND OF THE TWO MESHES SELECTED TO RUN MRE FINITE ELEMENT SIMULATIONS ON COMSOL MULTIPHYSICS® 5.3a. FOLLOWING ROWS: SPECIFICS ABOUT TRIANGULAR ELEMENTS FORMING THE MESHES.

Normal	*Finer*
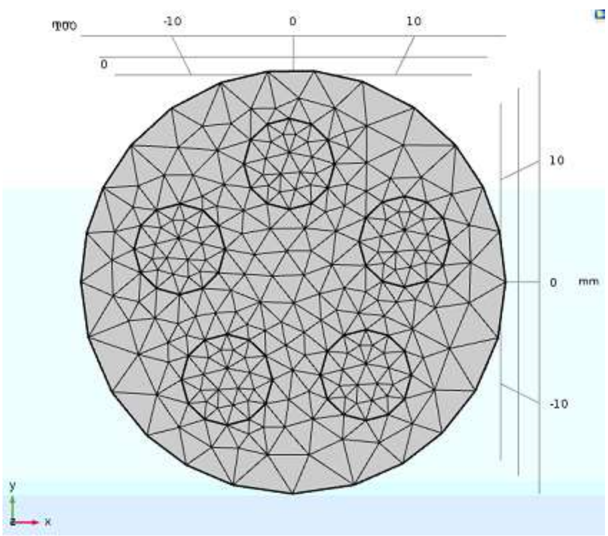	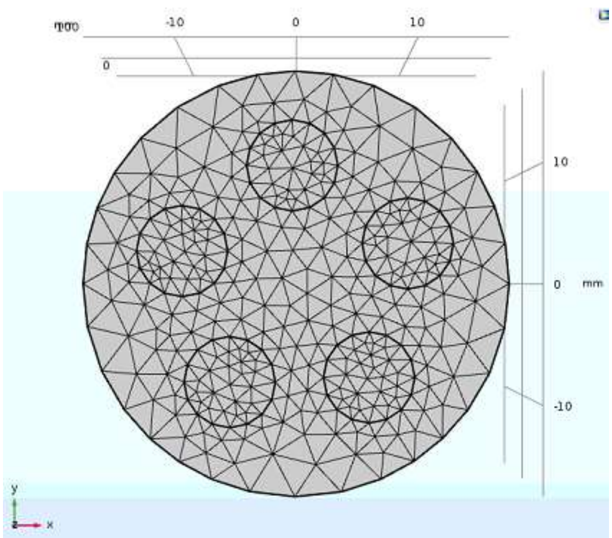
Number of elements: 49007	Number of elements: 148848
Shape of elements: triangular	Shape of elements: triangular

To better reproduce the boundary conditions applied to the Ecoflex™ sample in the *in vitro* MRE VeroClear 3D setup, a null displacement boundary condition is applied to both ends of the three-dimensional geometry in COMSOL Multiphysics® 5.3a. Moreover, a harmonic shear displacement of 11.6 µm amplitude boundary condition is applied uniformly to the whole lateral surface of the cylindric geometry. The simulation is run in the frequency domain at eight different mechanical excitation frequency values, ranging from 500 Hz to 4 kHz with a pace of 500 Hz between two consecutive frequencies.

CHAPTER 6

RESULTS AND DISCUSSION

6.1 <u>Overview of whole setup</u>

All the components of experimental setup are assembled with 4 mm diameter Nylon screws. Due to impossibility to machine a 1206.5 mm long holding tube at once, it is cut it at 720 mm from the end closer to the ROI. The portion of the tube cut away is replaced by a 486.5 mm Nylon rod, screwed to the cut border of the tube. Overall, the entire structure, including the tube and the rod, reaches 1206.5 mm in length, guaranteeing the position of ROI of the setup coincides with the ROI of the Agilent 9.4T 72 mm diameter RF coil. Figure 17 shows a top view of the assembled setup in its non-strained configuration (i.e. the phantom is held by clamps at 0% pre-strain).

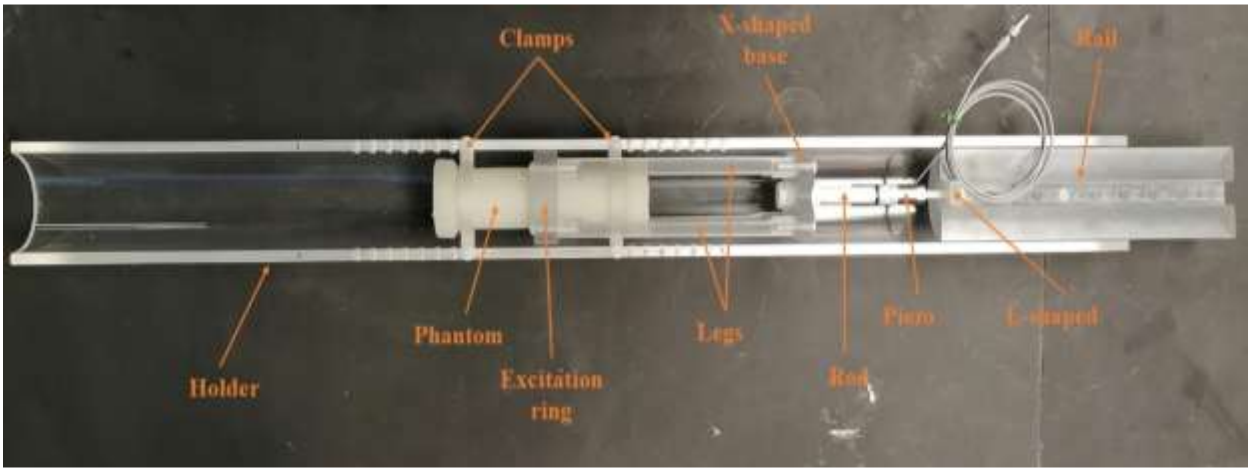

Figure 17: Top view of experimental setup, phantom included. To closely photograph the components of the setup, the 486.5 mm long Nylon rod is not included.

6.2 <u>Preliminary testing outcomes</u>

6.2.1 <u>Vibration Exciter</u>

The structure composed by piezo, rod, X-shaped parallelogram, four legs and excitation ring are screwed together and mounted to the Brüel & Kjær Vibration Exciter Type 4089 to test the effectiveness of transmission of vibration of the whole architecture.

Results of such preliminary testing are given in terms of acceleration transfer function (Figure 18). It relates acceleration of the two top accelerometers to the acceleration of the bottom accelerometer, which connects the Vibration Exciter to the whole structure. The two peaks over 10 dB in the transfer function graph are relative to the resonance frequencies of the system, at 704 Hz (Figure 18a) and 2544 Hz (Figure 18b). At such frequencies, output acceleration is considerably amplified with respect to input acceleration.

Figure 18: Acceleration transfer function from top to bottom of the piezo, rod, X-shaped base, legs and excitation ring structure. a) First peak larger than 10 dB, at 704 Hz. B) Second peak larger than 10 dB, at 2544 Hz.

The transfer function illustrates that for input signal frequencies below 2544 Hz, exception made for 704 Hz, the acceleration of the output, i.e. the excitation ring, is amplified by the setup with respect to the input acceleration. On the other hand, after the second resonance frequency, the magnitude of the transfer function decays below 0 dB. An explanation to such phenomenon could be found in setup acrylic material damping the amplitude of the acceleration at the higher frequencies.

6.2.2 Single Point Laser Doppler Vibrometry

The proper transmission of harmonic axial movement along the whole setup, including the phantom, is tested through the Single Point Laser Doppler Vibrometry. The ampler sinusoidal wave form visible on Tektronix TDS 210 Oscilloscope in Figure 19 represents the excitation ring harmonic velocity, driven by the velocity of the displacement imposed by the P-840.10 piezo actuator. The amplitudes of the sinusoids are 0.70 V for the excitation ring signal, and 0.25 V for the piezo.

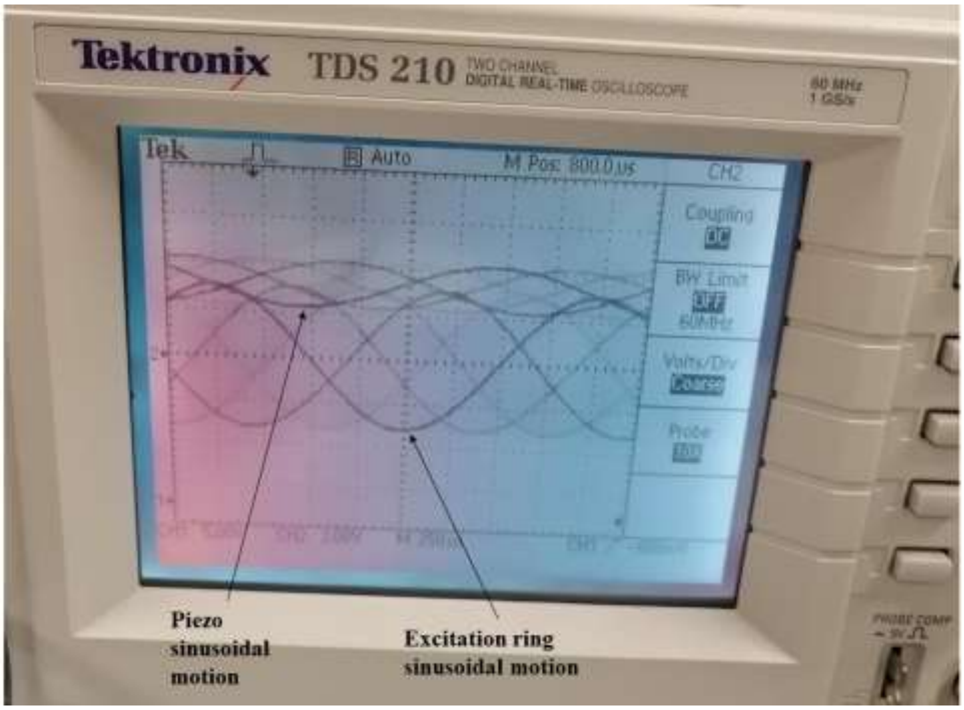

Figure 19: Harmonic displacement velocity signals of P-840.10 piezoelectric driver and excitation ring. The time frame displayed is 800 μs.

Consistently with the transfer function given by the Vibration Exciter (Figure 18), the setup seems to amplify the harmonic displacement velocity magnitude by a factor greater that 0 dB, but littler than 10 dB, when the piezo driver is triggered. A constant phase shift of about $\pi/2$ is observed between input and output signal.

6.1 <u>MRE in Agilent 9.4 T</u>

One single experiment is conducted with the 9.4 T Agilent coil. Mechanical driving frequency is set at 500 Hz, and no pre-strain is applied to the phantom. Ten 1 mm thick slices are acquired and the postprocessing analysis is made on the fifth slice.

Magnitude image in Figure 19 clearly depicts the external matrix and fibers domains within the axial slice. However, it reveals also some air entrapped between external matrix and fibers domains, as there is discontinuity in signal at the interface. The presence of air at the boundary might be due to a poor sticking of liquid Ecoflex™ 0030 to solidified Ecoflex™ 0010 when poured and left curing.

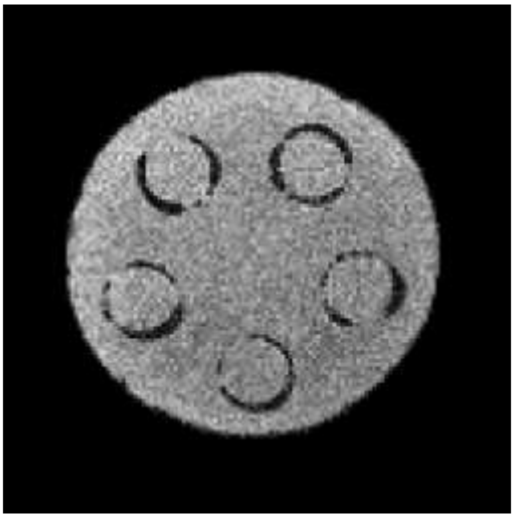

Figure 20: MR magnitude image of the phantom, taken with Agilent 9.4 T using 72 mm diameter RF coil. The lacking signal at matrix-fibers interface could be caused by air entrapped in.

Unwrapped phase image illustrates the real part of the complex shear waves propagating within the sample (Figure 20). Flynn algorithm is used to unwrap the image.

Half a wavelength is visible, beginning from the top right portion of the circumference of the phantom to the center of convergence. Moreover, no scattering of the wave is observed at the external matrix-fibers interface, which should be indicated by the different shear stiffness of the typologies of Ecoflex™ composing matrix and fibers eventually.

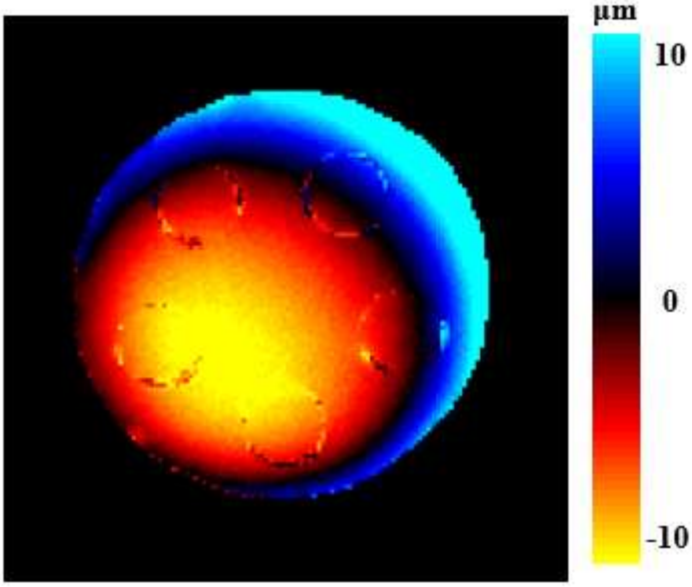

Figure 21: MR unwrapped phase image of the phantom, taken with the Agilent 9.4 T using 72 mm diameter RF coil. The wave front does not converge to the center of the phantom cross-section, when axial symmetry should imply convergence in the middle of the slice. No wave scattering is present.

A convergent and slightly elliptic wave front is visible, even though the convergence point is not located close to the geometric center of the cross-section, as axial symmetry of the sample would suggest instead. In experimental conditions, a non-perfect matching of point of convergence with center of the slice could be understood. In the present case, the offset is 7 mm large, and such distance coincides with the 20% of the diameter of the phantom. Therefore, the presence of a wide the offset might be indicating a non-uniform grip of the excitation ring around the circumference, as the waves seem to be generated only at the rightmost half of the phantom.

6.2 <u>COMSOL Multiphysics 5.3a simulations</u>

To predict how the presence of stiffer fiber domains influence the propagation of shear waves in a softer matrix, a longitudinally pre-strained MRE experiment is simulated in COMSOL Multiphysics 5.3a. A direct problem is assessed, since knowing the viscoelastic properties of the materials the aim of the computational investigation is to examine the diffusion of mechanical shear waves. Operating in the frequency domain, the addressed viscoelastic properties are frequency dependent. Complex-valued shear and bulk moduli account for both elasticity and damping in the phantom 3D model in COMSOL Multiphysics® 5.3a.

The results of the simulations are presented in eight tables, one for each frequency of excitation at the boundary of the geometry. Every table includes the resultant wave image from a specific frequency and axial pre-strain applied. The wave images represent displacement along directions parallel to z axis, generated by z axis-polarized harmonic shear displacement at the boundary. Axial displacement in each image is in mm.

At the first three excitation frequencies applied (500 Hz, 1000 Hz, and 1500 Hz), no or little difference is noticeable between shear waves propagating at the four different pre-strain values. Coherently with expression (4.1), the wavelength seems to increase as excitation frequency rises.

TABLE IV: COMSOL COMPUTATIONAL WAVE IMAGES AT 500 Hz EXCITATION FREQUENCY. MESH USED IS “NORMAL”.

Pre-strain applied	Wave image
0%	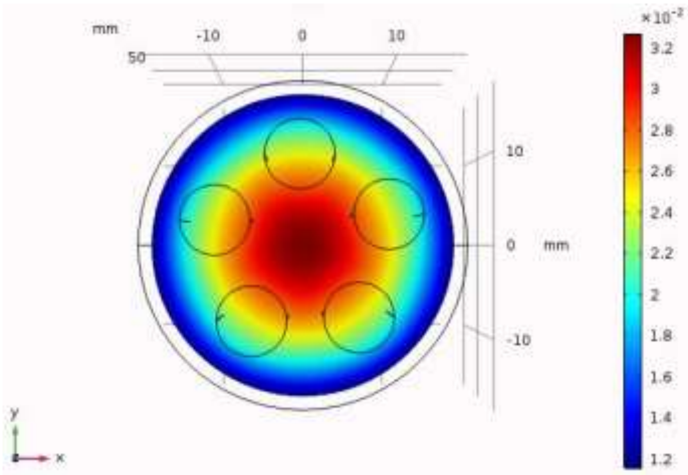

10%	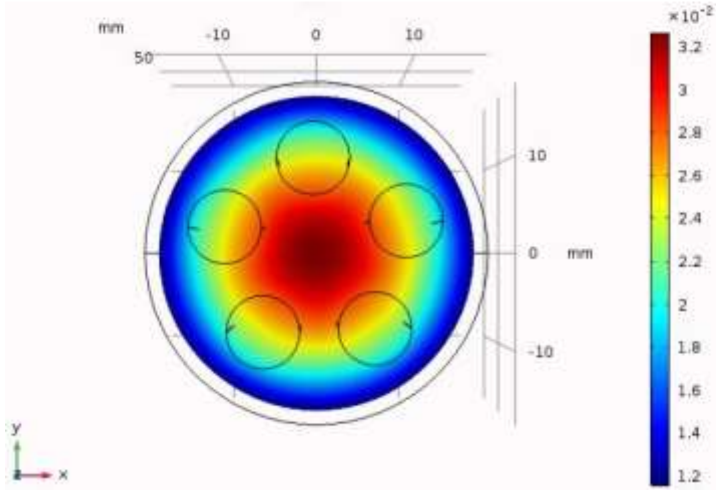
20%	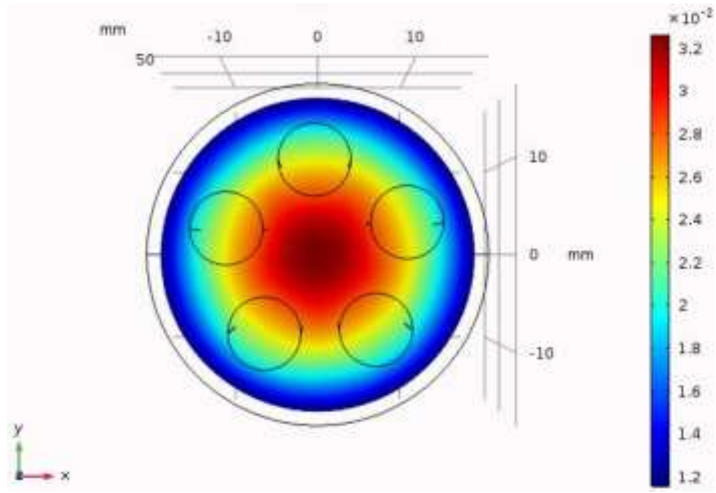
50%	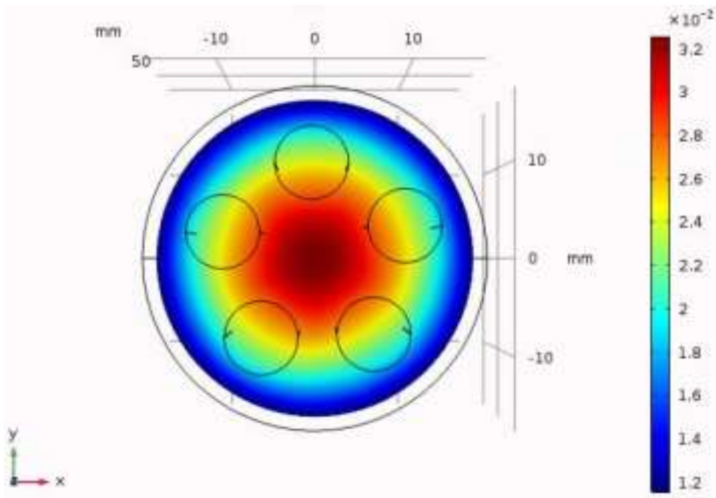

While at 500 Hz the wave front appears to be circular, therefore with the stiffer fibers having no substantial effect on propagation speed, from 1000 Hz onwards the influence of the five cylindrical fibers is minimally visible (TABLE V and TABLE VI). Indeed, on the axial plane, in the radial directions across the fibers, the wavelength is slightly longer in comparison with wavelength in the spaces where the inward propagating wave front does not hit the fibers.

TABLE V: COMSOL COMPUTATIONAL WAVE IMAGES AT 1000 Hz EXCITATION FREQUENCY. MESH USED IS “NORMAL”.

Pre-strain applied	Wave image
0%	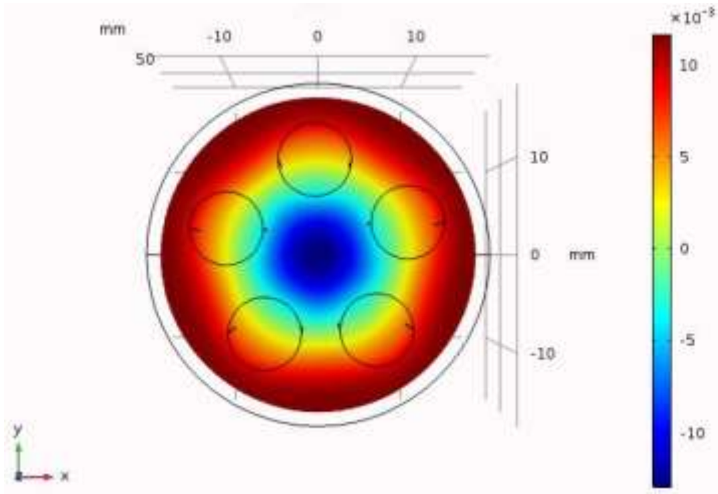
10%	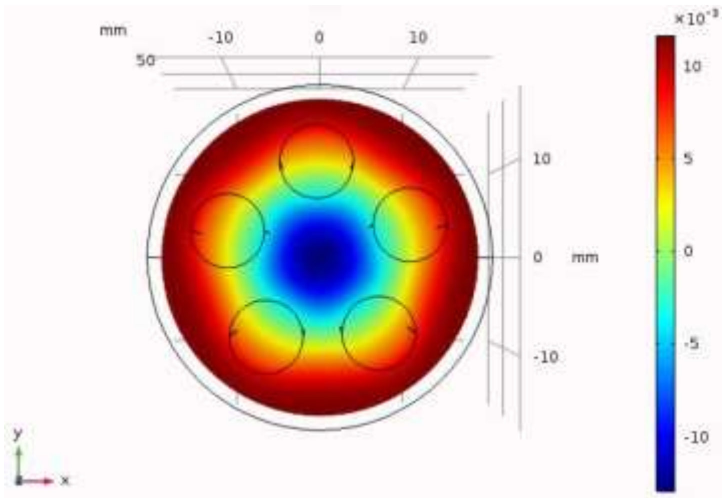

20%	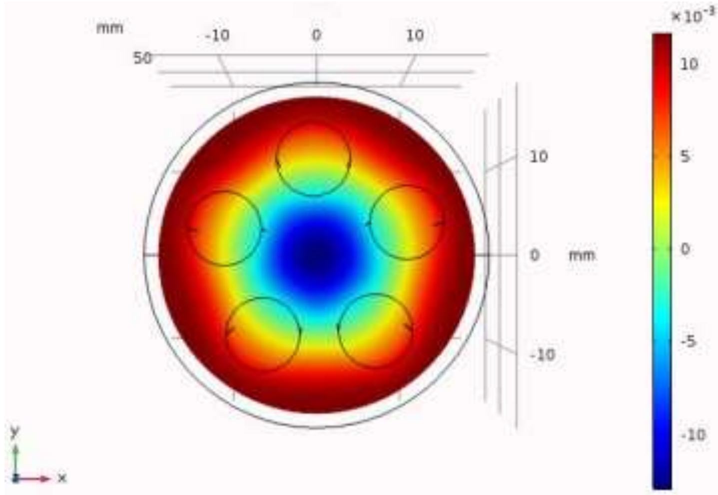mm -10 0 10 50 10 0 mm -10 ×10⁻³ 10 5 0 -5 -10 y x
50%	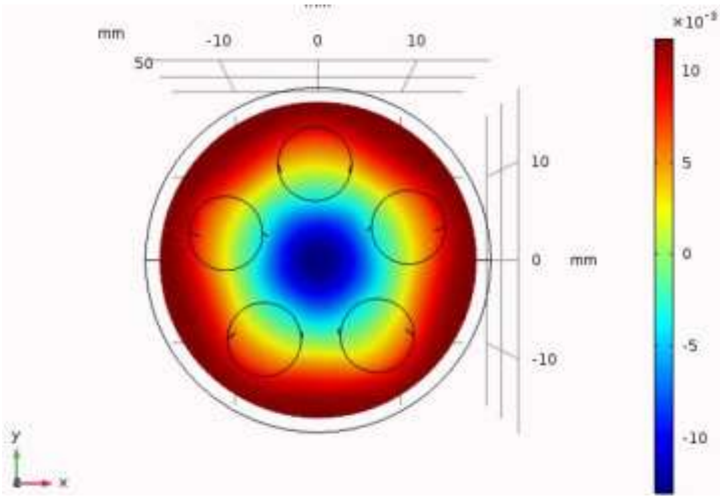mm -10 0 10 50 10 0 mm -10 ×10⁻³ 10 5 0 -5 -10 y x

TABLE VI: COMSOL COMPUTATIONAL WAVE IMAGES AT 1500 Hz EXCITATION FREQUENCY. MESH USED IS "NORMAL".

Pre-strain applied	Wave image
0%	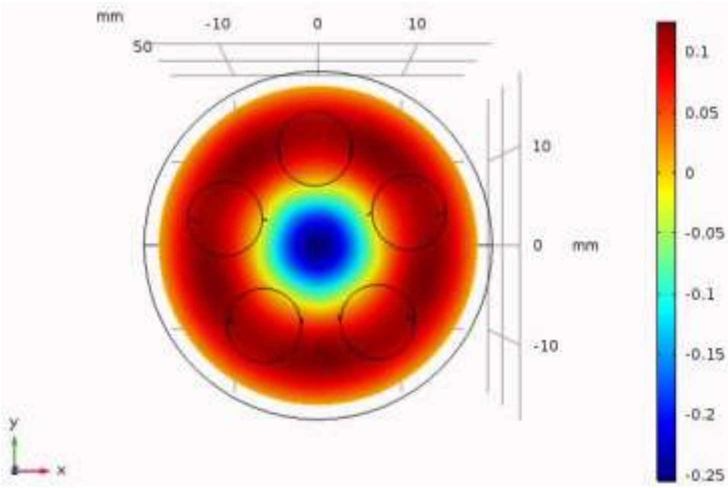
10%	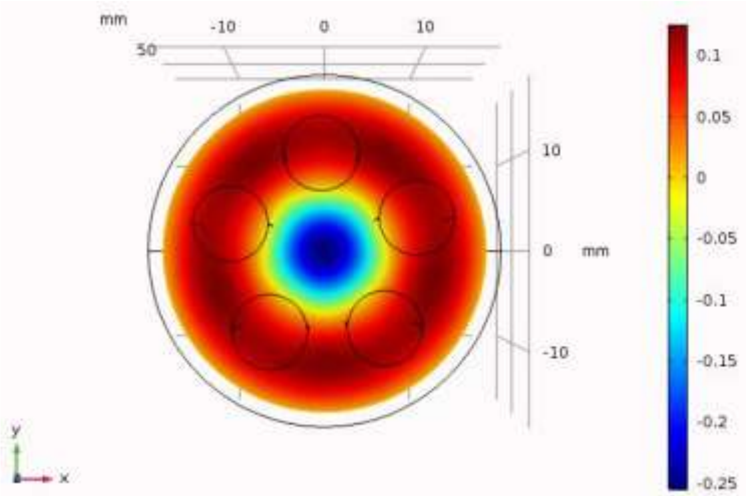
20%	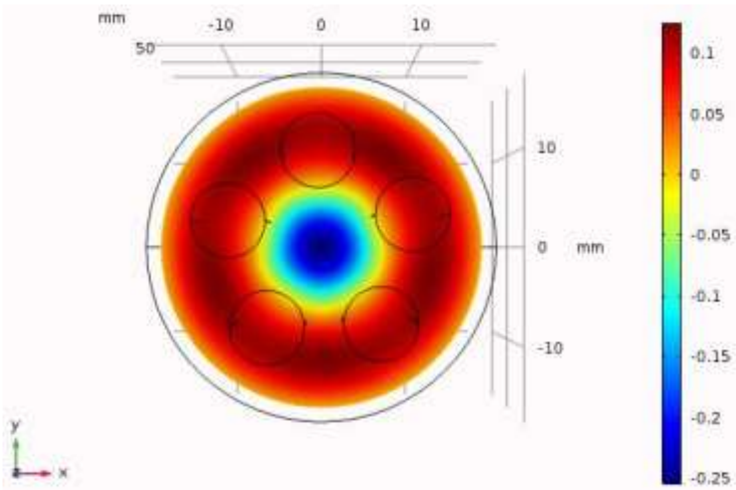

50%	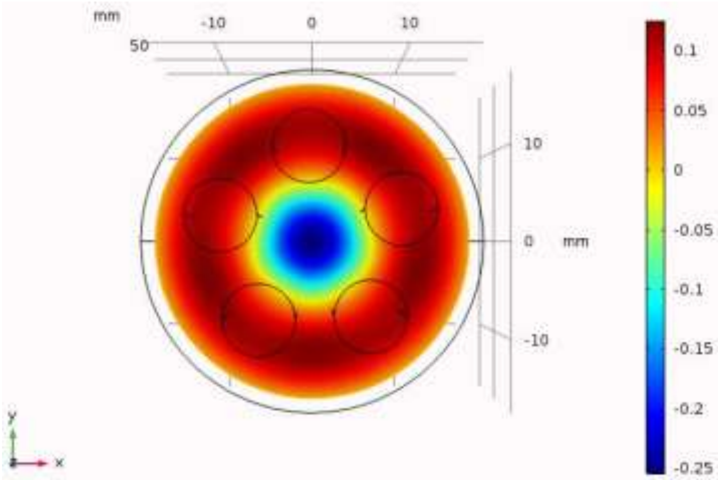

Even though there is not a considerable variation in the wave image among the four pre-strain values, at 2000 Hz the enlargement of the wavelength within the fibers is clearer. Almost three quarters of a wavelength are visible. Only at 50% of pre-strain the axial symmetry of the wave front seems perturbated, maybe due to mesh imprecisions. In correspondence of radial direction of fibers, the displacement does not reach a maximum displayed value, approximately equal to $15 x 10^{-3}$ mm, but stops at $10 x 10^{-2}$ mm. This phenomenon underscores how stiffer fibers determine a wider λ in correlation with matrix-only radial direction of propagation.

TABLE VII: COMSOL COMPUTATIONAL WAVE IMAGES AT 2000 Hz EXCITATION FREQUENCY. MESH USED IS "NORMAL".

Pre-strain applied	Wave image
0%	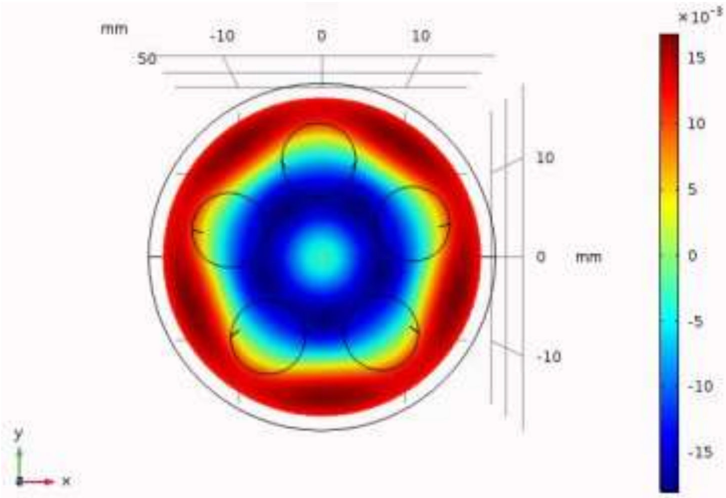
10%	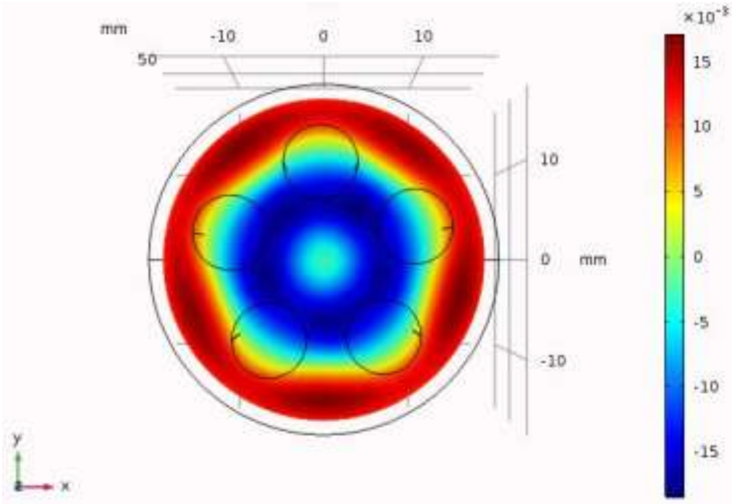
20%	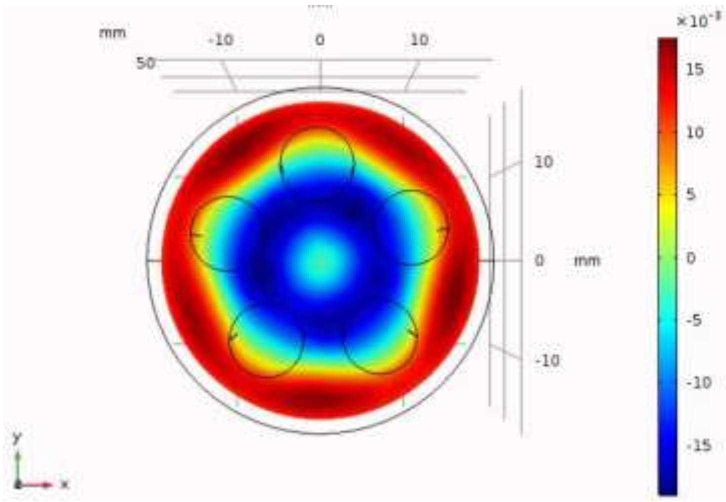

50%	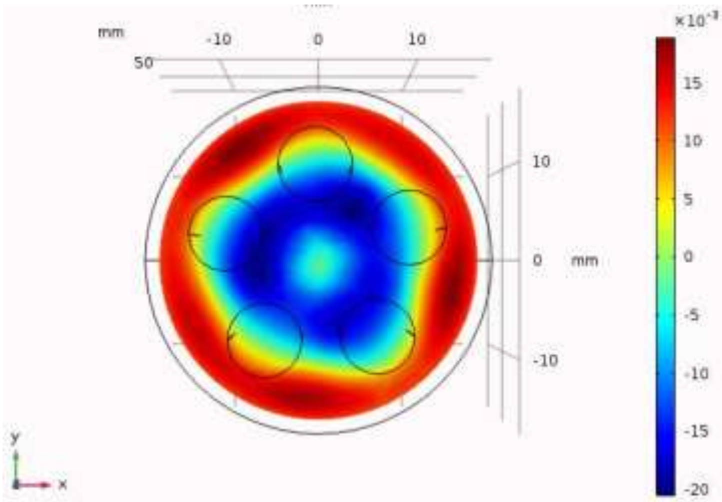

From 2500 Hz onwards, axial displacement gains shapes never detected in previous works as well as in the lower frequencies of the present study. Supposing a concentric wave front, as in the previous frequencies, this does not look to lie on a plane parallel to the cross-section but acquires a sinusoidal shape, oscillating in and out of the axial plane. The amplitude of the mentioned sinusoid varies with the radial distance, decaying to zero when the radial distance is shorter than the distance between the center and the circumference of the fibers. Past the fibers, the wave front takes on a planar shape.

TABLE VIII: COMSOL COMPUTATIONAL WAVE IMAGES AT 2500 Hz EXCITATION FREQUENCY. MESH USED IS "NORMAL".

Pre-strain applied	Wave image
0%	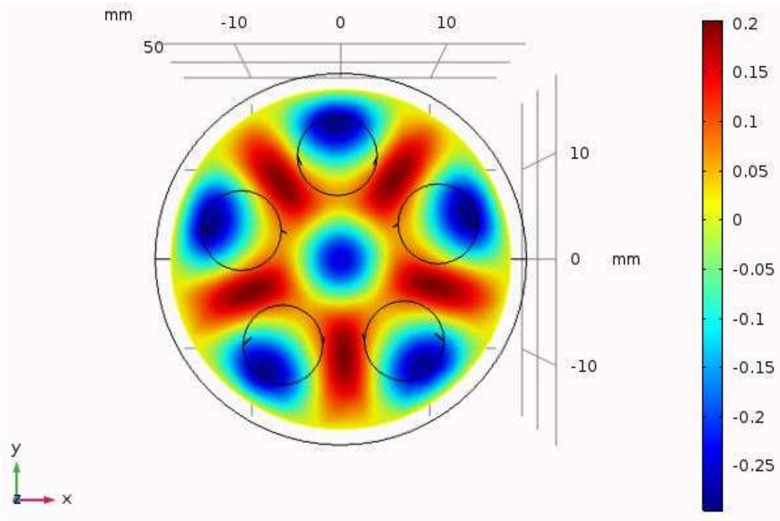
10%	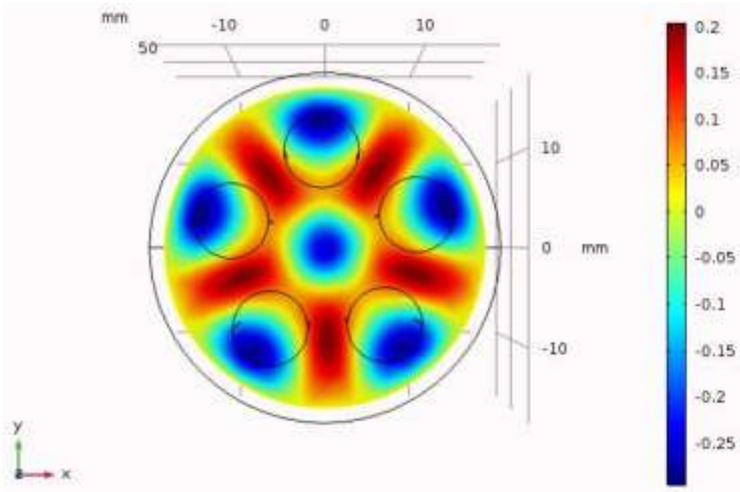
20%	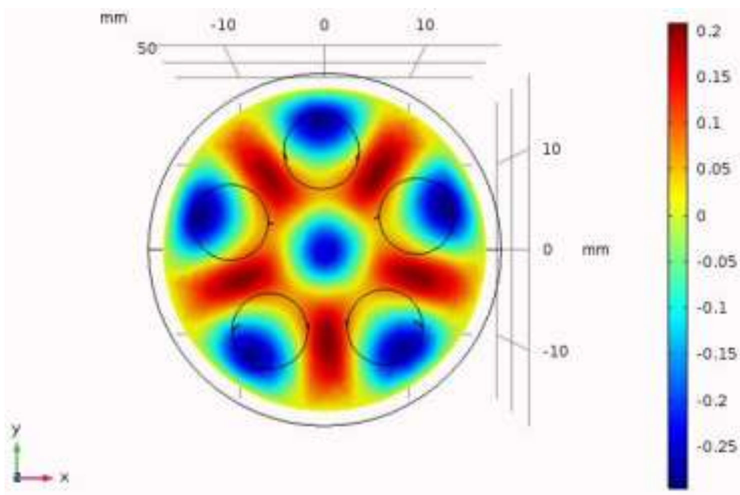

50%	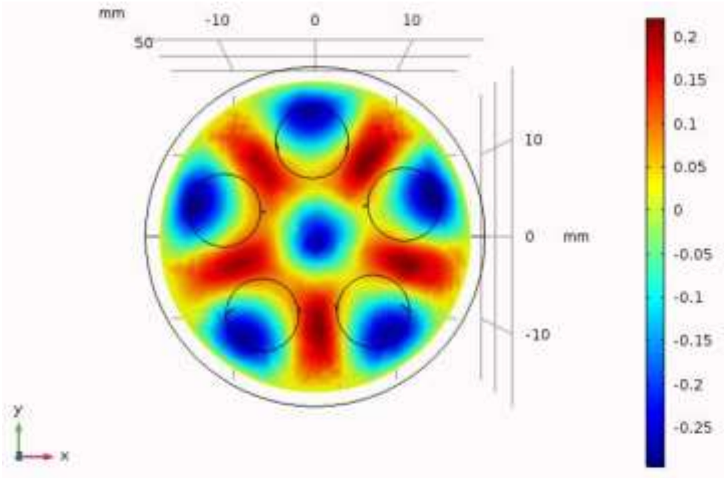

A similar wave pattern to that observed at 2500 Hz characterizes images at 3000 Hz, holding the symmetry with respect to the axis of the phantom. Again, a concentric wave front appears to be sinusoidal, becoming planar only when the radial distance is smaller than the distance of fibers circumference from the central point of the slice. Moreover, the wave image at 50% looks substantially different from those at lower strain values. Displacement amplitude presents 1.8 mm “coupled” peaks for each fiber, while being close to 0 mm elsewhere on the cross-section. A possible explanation to that event might lie in the increased damping occurring at higher frequencies, or in the progressive shielding effect the fibers have on the propagation of convergent waves. Indeed, the lobes do not propagate towards the center: the shear waves seem to get damped progressively when moving inwards.

TABLE IX: COMSOL COMPUTATIONAL WAVE IMAGES AT 3000 Hz EXCITATION FREQUENCY. MESH USED IS "FINER".

Pre-strain applied	Wave image
0%	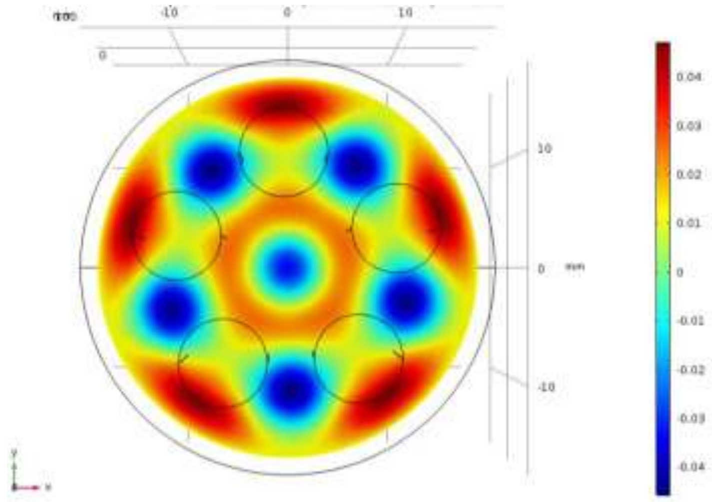
10%	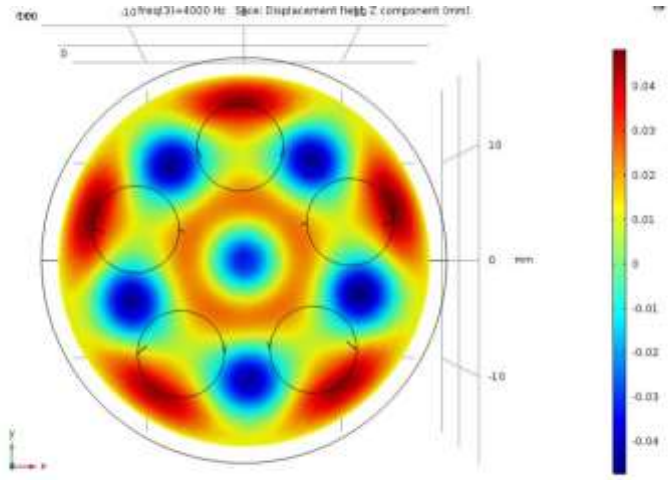

20%	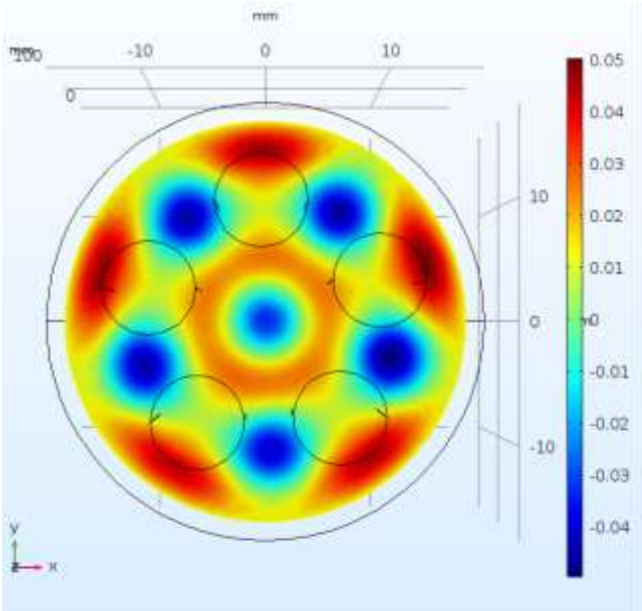
50%	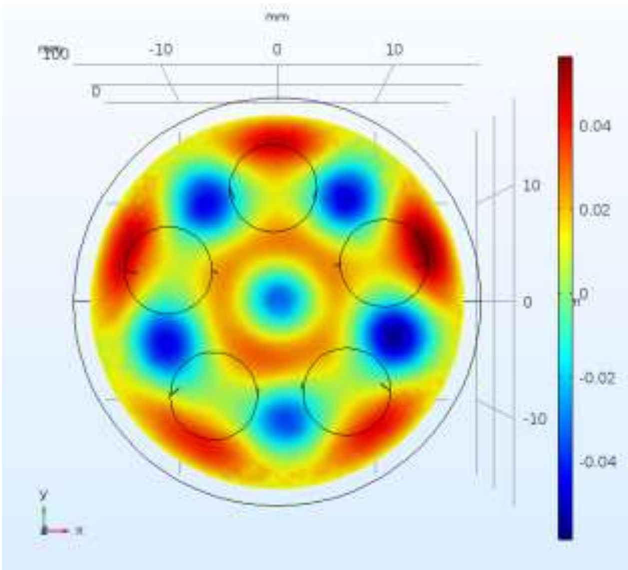

Also, images obtained at 3500 Hz suggest an enlargement of wavelength when shear waves traverse Ecoflex™ 0030 fibers. In the x,y plane, while along directions not hitting the fibers almost two full wavelengths are visible, in the fibers z-displacement appears to be slowly reaching negative values. Axial symmetry of the wave patterns is kept also at 3500 Hz.

Blurring characterizes increasingly the images at 10%, 20% and 50% prestrain. A finer mesh might be helpful in better resolving those images. Nonetheless, it is still distinguishable a wave pattern resembling that developed at 0% pre-strain.

Due to the difference between the three images at 0%, 10%, 20% and the picture at 50% pre-elongation, it could be inferred that pre-strain begins to influence significantly shear waves propagation only after a certain threshold in terms of both axial deformation and vibration frequency. Eventually, at 50% pre-strain value, damping might play a major role in determining the progressively decreasing amplitude of displacement over the cross section.

TABLE X: COMSOL COMPUTATIONAL WAVE IMAGES AT 3500 Hz EXCITATION FREQUENCY. MESH USED IS "FINER".

Pre-strain applied	Wave image
0%	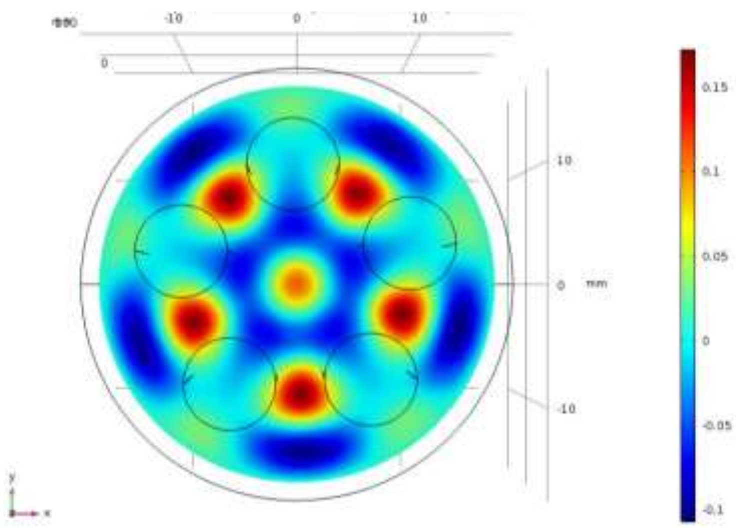

10%	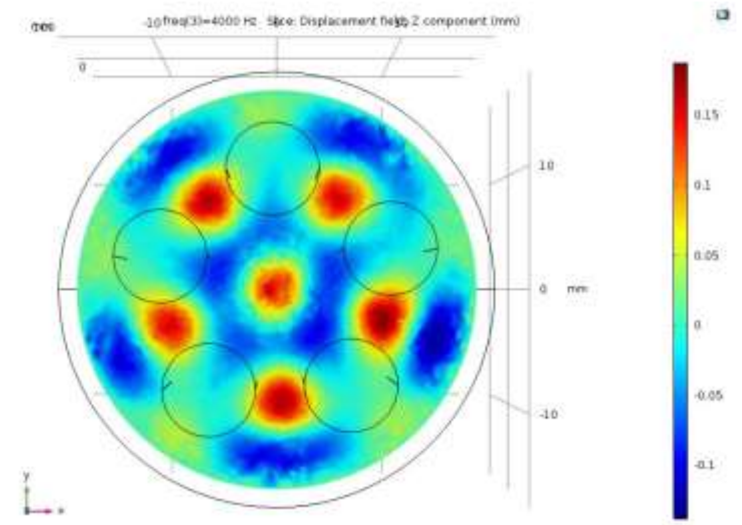freq(3)=4000 Hz Slice: Displacement field, Z component (mm) -10 0 10 0 mm -10 0.15 0.1 0.05 0 -0.05 -0.1 y x
20%	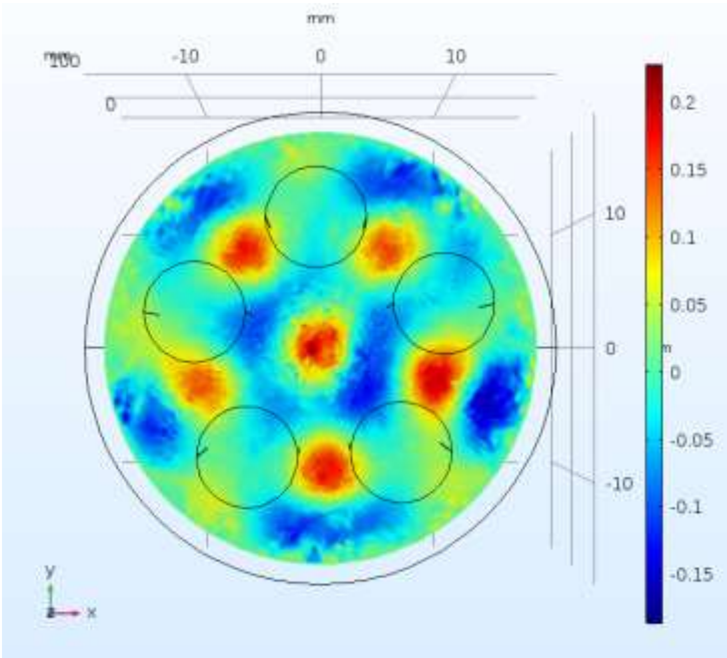mm -10 0 10 0 10 0 -10 0.2 0.15 0.1 0.05 0 -0.05 -0.1 -0.15 y x

50%	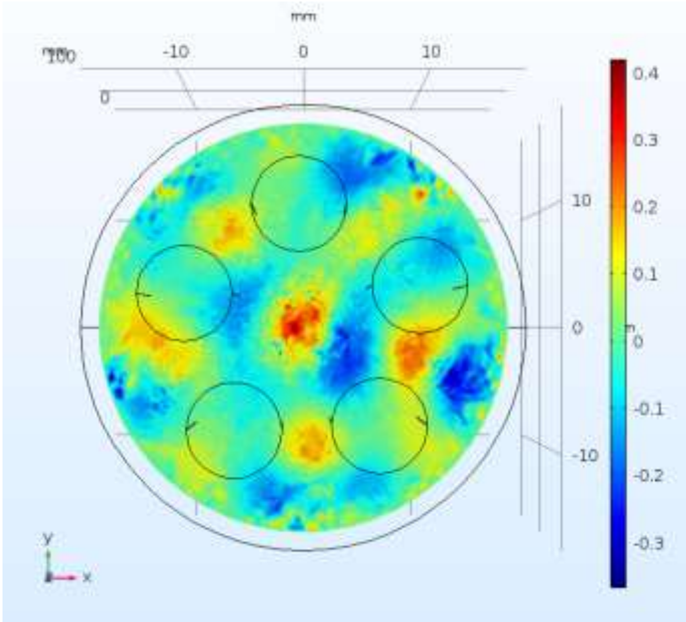

Lastly, simulations at 4000 Hz are analyzed. Dissimilarly from the precedent frequencies, at 4 kHz pre-strain appears to weigh more on the wave propagation pattern. On a circular annulus spanning from the outer boundary to the circumference where the centers of fibers sections lay on, the wave front possesses a sinusoidal shape higher in angular frequency if compared to precedent frequencies. Furthermore, as the geometry gets stretched, damping becomes more visible: displacement magnitude decays to nearly 0 mm at the center of the cross section. This would support the theory of strengthened damping effects on shear waves propagation as mechanical stimulation frequency rises. As previously reported, a shielding effect provided by the geometry of the phantom could further influence the inward propagation of the wave.

TABLE XI: COMSOL COMPUTATIONAL WAVE IMAGES AT 4000 Hz EXCITATION FREQUENCY. MESH USED IS "FINER".

Pre-strain applied	Wave image
0%	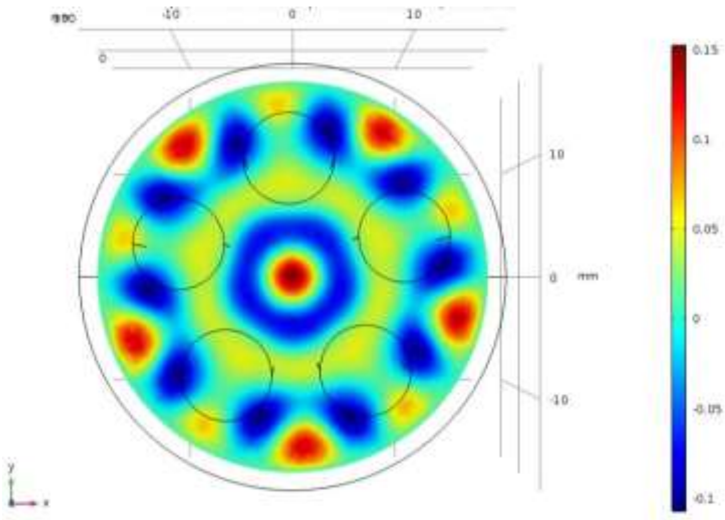
10%	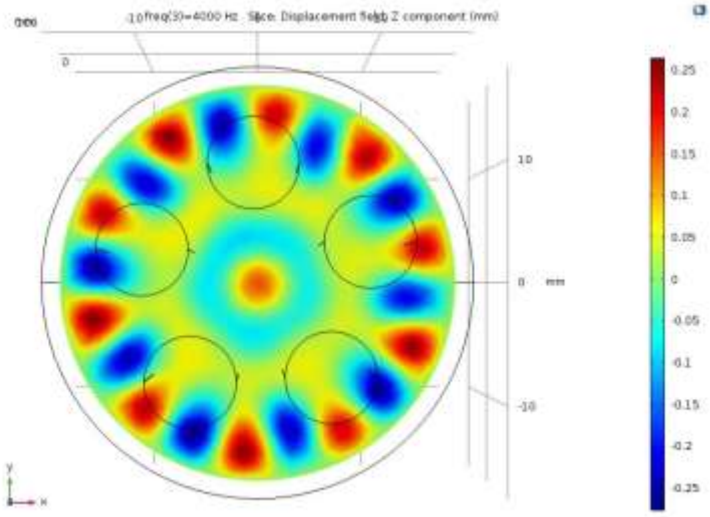

20%	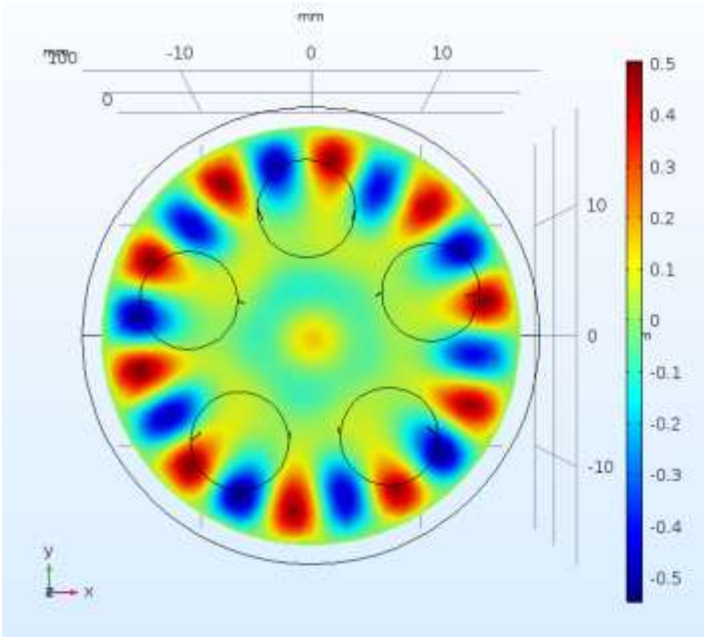
50%	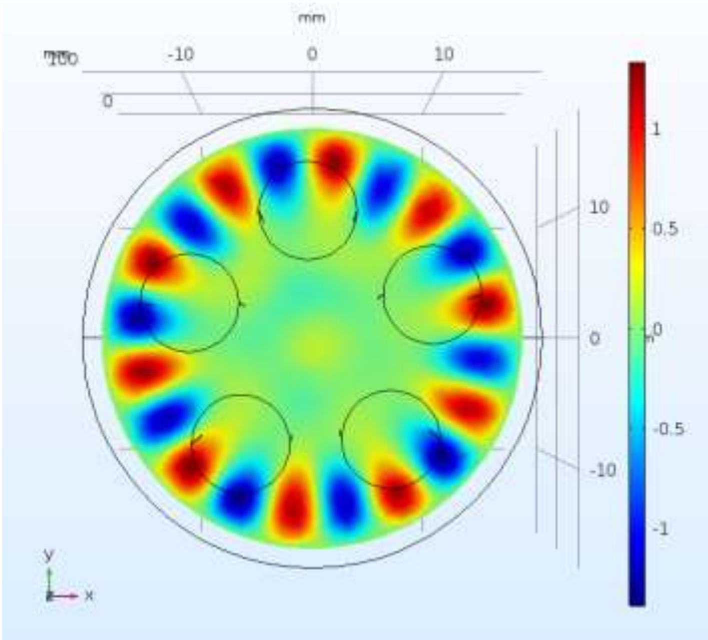

The sinusoidal wave front observable at 2500 – 4000 Hz frequency range might be generated by scattering and reflection phenomena happening in proximity of boundaries between matrix and fibers domains. There might exist also a reflection of waves being by the fixed phantom extrema which would have an influence in determining such patterns, even though their contribute would result less relevant with respect to in-plane matrix-fibers boundaries as the phantom geometry aspect ratio is 0.35.

The effect of pre-strain is not yet too evident from the COMSOL Multiphysics 5.3a simulations run, even though stiffening seems to take place as wavelengths increase when reaching higher values of pre-stretching. It may come to the interest of a future study to further expand longitudinal pre-strain, getting to 100% or more of resting length phantom [39].

CHAPTER 7

CONCLUSION AND FUTURE DEVELOPMENTS

Magnetic Resonance Elastography has acquired an increasing interest for its ability to investigate mechanical properties of tissues noninvasively and independently from intra- and inter-operator factors [1]. Specifically, the most recent studies on MRE applied to skeletal muscle are aiming at better understanding not only how pathologies affect viscoelastic properties of the tissue, but also at gaining deeper insights of how a passive and active tension might influence muscle stiffness in physiological condition [1][7][8]. The identification of shear stiffness in MRE is achieved by means of inversion algorithms. They exploit motion-sensitive Magnetic Resonance Imaging data to determine the distribution of frequency-dependent complex shear modulus within the tissue investigated [12].

Parallelly to experimental MRE, Finite Element Analysis employs a direct problem approach to explore how both anisotropy and known viscoelastic properties affect the propagation of induced shear waves. Assessing stationary propagation of shear waves with computational simulations allows to predict quickly and precisely how materials and anisotropic geometries influence the diffusion of waves within a sample. In this sense, FE experiments might help in improving inversion algorithms: minimizing an error function defined as the difference between FEA determined displacement field and experimental MRE displacement field could support a deeper understanding of the precision and the accuracy of the specific inversion algorithm used.

The present work has multiple purposes: to build a phantom mimicking the basic structure of skeletal muscle; to develop and test an experimental setup allowing simultaneously to apply axially pre-strain boundary conditions to the sample and provide it with mechanical harmonic stimulation driven by a piezo actuator; to computationally perform simulations aiming at predicting how known viscoelastic properties of a material might alter propagation of axially-polarized shear waves.

Since still little literature can be found about how passive tension in skeletal muscles influences their mechanical features [39], both in physiological and pathological conditions, the development of a transversely isotropic phantom and its elastographic analysis was addressing a deeper insight on how pre-tension could affect shear waves modes and their propagation.

As observable in the tables included in chapter 6, too little difference exists between the wave patterns at diverse pre-strains. One future development might be the production and MRE analysis of a phantom having stiffer fibers. A possible material in this sense could be represented by Ecoflex™ 0050 or silicon rubbers of the same tensile strength range. In this way, one would increase the discrepancy between matrix and fibers domain bulk and shear moduli, consequently being able to distinguish more clearly how the variation in stiffness along the direction of propagation of the wave disturbs the propagation itself.

Moreover, the pouring process of liquid Ecoflex™ should be executed carefully. Entrapped air between fibers and matrix domains should not be present. To make sure no air remains in between the two materials, a potential development could be to tight seal in vacuum the phantom with empty fibers, and to pour liquid Ecoflex™, or another material designed to simulate fibers, punching a small hole with a syringe so that as little air as possible enters.

Undoubtedly, it will be essential to understand how increasing excitation frequencies, together with scattering and reflection phenomena, cause profound diversification of shear wave modes, as noticeable in TABLE IX, TABLE X and TABLE XI.

Both in experimental and in FEA environment it is still yet to be derived a tradeoff between the optimal stimulation frequency and the damping intrinsic in a viscoelastic model. While higher frequencies hold a shorter wavelength, at the incidence of damping arises, preventing inward propagation of shear waves.

CITED LITERATURE

[1] Y. K. Mariappan, K. J. Glaser, and Richard L Ehman, “Magnetic Resonance Elastography: a Review,” *Clin. Anat.*, vol. 23, no. 5, pp. 497–511, 2010.

[2] P. Asbach *et al.*, “Viscoelasticity-based staging of hepatic fibrosis with multifrequency MR elastography,” *Radiology*, vol. 257, no. 1, pp. 80–86, 2010.

[3] L. Huwart *et al.*, “Liver fibrosis: Non-invasive assessment with MR elastography,” *NMR Biomed.*, vol. 19, no. 2, pp. 173–179, 2006.

[4] M. C. Murphy *et al.*, “Decreased brain stiffness in Alzheimer’s disease determined by magnetic resonance elastography,” *J. Magn. Reson. Imaging*, vol. 34, no. 3, pp. 494–498, 2011.

[5] J. P. Emmanuel, N., Callé, S., Remenieras, “Generating shear waves in the human brain for ultrasound elastography: a new approach,” *Phys. Procedia*, 2015.

[6] L. Xu *et al.*, “Assessment of stiffness changes in the ex vivo porcine aortic wall using magnetic resonance elastography,” *Magn. Reson. Imaging*, vol. 30, no. 1, pp. 122–127, 2012.

[7] R. L. Lieber, S. Steinman, I. A. Barash, and H. Chambers, “Structural and functional changes in spastic skeletal muscle,” *Muscle and Nerve*, vol. 29, no. 5, pp. 615–627, 2004.

[8] M. a Alnaqeeb, N. S. Al Zaid, and G. Goldspink, “Connective tissue changes and physical properties of developing and ageing skeletal muscle.,” *J. Anat.*, vol. 139 (Pt 4, pp. 677–689, 1984.

[9] J. R. Basford, T. R. Jenkyn, K. N. An, R. L. Ehman, G. Heers, and K. R. Kaufman, “Evaluation of healthy and diseased muscle with magnetic resonance elastography,” *Arch. Phys. Med. Rehabil.*, vol. 83, no. 11, pp. 1530–1536, 2002.

[10] M. a Dresner, G. H. Rose, P. J. Rossman, R. Muthupillai, a Manduca, and R. L. Ehman, “Magnetic resonance elastography of skeletal muscle.,” *J. Magn. Reson. Imaging*, vol. 13, pp. 269–276, 2001.

[11] C. G. Nudo *et al.*, “Correlation of laparoscopic liver biopsy to elasticity measurements (FibroScan) in patients with chronic liver disease,” *Gastroenterol. Hepatol.*, vol. 4, no. 12, pp. 862–870, 2008.

[12] S. Hirsch, J. Braun, and I. Sack, *Magnetic Resonance Elastography Physical Background and Medical Applications*, First. Weinheim, Germany: Wiley-VCH Verlag GmbH & Co. KGaA, 2017.

[13] T. K. Liu, Yifei, Yasar, T. J. Royston, and R. L. Magin, “Ultra Wideband (0.5 – 16 kHz) MR Elastography for Robust Shear Viscoelasticity Model Identification,” *Magn. Reson. Med.*, vol. 70, no. 2, pp. 479–489, 2013.

[14] R. L. Kruse, Scott A., Rose, Gregory H., Glaser, Kevin J., Manduca, Armando, Felmlee, Joel P., Jack, Clifford R., Ehman, “Magnetic Resonance Elastography of the Brain,” *Neuroimage*, vol. 11, no. 5, pp. 447–453, 2009.

[15] P. Y. Xu, L., Lin, Y., Han, J. C., Xi, Z. N., Shen, H., Gao, “Magnetic resonance elastography of brain tumors: preliminary results,” *Acta radiol.*, 2007.

[16] S. K. Venkatesh, M. Yin, and R. L. Ehman, “Magnetic resonance elastography of liver: Technique, Analysis, and Clinical applications,” *J. Magn. Reson. Imaging*, vol. 37, no. 6, pp. 887–896, 2013.

[17] B. C. Goss, K. P. McGee, E. C. Ehman, a Manduca, and R. L. Ehman, “Magnetic resonance elastography of the lung: technical feasibility.,” *Magn. Reson. Med.*, vol. 56, no. 5, pp. 1060–1066, 2006.

[18] P. R. Moran, “A flow velocity zeugmatographic interlace for NMR imaging in humans,”

Magn. Reson. Imaging, vol. 1, no. 4, pp. 197–203, 1982.

[19] R. Muthupillai, D. J. Lomas, P. J. Rossman, J. F. Greenleaf, A. Manduca, and R. L. Ehman, “Magnetic resonance elastography by direct visualization of propagating acoustic strain waves,” *Science (80-.).*, vol. 269, no. 5232, pp. 1854 LP – 1857, Sep. 1995.

[20] L. Sandrin *et al.*, “Transient elastography: a new noninvasive method for assessment of hepatic fibrosis.,” *Ultrasound Med. Biol.*, vol. 29, no. 12, pp. 1705–1713, 2003.

[21] K. F. Graff, *Wave Motion in Elastic Solids*. 1991.

[22] A. Bedford and D. S. Drumheller, *Introduction to Elastic Wave Propagation*. 1996.

[23] Y. Zheng *et al.*, “Shear Wave Propagation in Soft Tissue and Ultrasound Vibrometry,” *Intech*, 2013.

[24] S. Goss, R. Johnston, and S. Shnol, “Comprehensive compilation of empirical ultrasonic properties of mammalian tissues.,” *J Acoust Soc Am*, vol. 64, no. 2, pp. 423–57, 1978.

[25] G. Muller, *Theory of elastic waves*. 2007.

[26] a. Manduca *et al.*, “Magnetic resonance elastography: Non-invasive mapping of tissue elasticity,” *Med. Image Anal.*, vol. 5, no. 4, pp. 237–254, 2001.

[27] R. Sinkus *et al.*, “Imaging anisotropic and viscous properties of breast tissue by magnetic resonance-elastography,” *Magn. Reson. Med.*, vol. 53, no. 2, pp. 372–387, 2005.

[28] S. Federico, A. Grillo, and S. Imatani, “The linear elasticity tensor of incompressible materials,” vol. 20, no. 6, pp. 643–662, 2015.

[29] J. M. Carcione, D. Kosloff, and R. Kosloff, “Wave propagation simulation in a linear viscoelastic medium,” *Geophys. J.*, vol. 95, no. 1988, pp. 597–611, 1988.

[30] T. E. Oliphant, A. Manduca, R. L. Ehman, and J. F. Greenleaf, “Complex-valued stiffness reconstruction for magnetic resonance elastography by algebraic inversion of the

differential equation," *Magn. Reson. Med.*, vol. 45, no. 2, pp. 299–310, 2001.

[31] T. E. Oliphant, J. L. Mahowald, R. L. Ehman, J. F. Greenleaf, and M. Foundation, "Measurements and Local Inversion of Conservation of Moment Um," pp. 1641–1644, 1999.

[32] R. Howard, A., Chris, *Elementary Linear Algebra*. 2005.

[33] F. H. Martini, M. J. Timmons, R. B. Tallitsch, W. C. Ober, and C. W. Garrison, *Human Anatomy*, 6th ed. 2008.

[34] G. J. Tortora and M. T. Nielsen, *Principles of Human Anatomy*, vol. 53, no. 9. 2012.

[35] S. S. Blemker and S. L. Delp, "Three-dimensional representation of complex muscle architectures and geometries," *Ann. Biomed. Eng.*, vol. 33, no. 5, pp. 661–673, 2005.

[36] D. A. Morrow, T. L. Haut Donahue, G. M. Odegard, and K. R. Kaufman, "Transversely isotropic tensile material properties of skeletal muscle tissue," *J. Mech. Behav. Biomed. Mater.*, vol. 3, no. 1, pp. 124–129, 2010.

[37] S. Papazoglou, J. Rump, J. Braun, and I. Sack, "Shear wave group velocity inversion in MR elastography of human skeletal muscle," *Magn. Reson. Med.*, vol. 56, no. 3, pp. 489–497, 2006.

[38] B. A. Auld, *Acoustic fields and waves in solids*, vol. 8, no. 1. 1975.

[39] S. Brinker and D. Klatt, "Demonstration of concurrent tensile testing and magnetic resonance elastography," *J. Mech. Behav. Biomed. Mater.*, vol. 63, pp. 232–243, 2016.

[40] R. L. Yasar, Temel K., Royston, Thomas J., Magin, "Wideband MR elastography for viscoelasticity model identification," vol. 100, no. 2, pp. 130–134, 2012.

[41] D. Klatt, S. Papazoglou, J. Braun, and I. Sack, "Viscoelasticity-based MR elastography of skeletal muscle," *Phys. Med. Biol.*, vol. 55, no. 21, pp. 6445–6459, 2010.

[42] I. Sack *et al.*, “The impact of aging and gender on brain viscoelasticity,” *Neuroimage*, vol. 46, no. 3, pp. 652–657, 2009.

[43] J. Wuerfel *et al.*, “MR-elastography reveals degradation of tissue integrity in multiple sclerosis,” *Neuroimage*, vol. 49, no. 3, pp. 2520–2525, 2010.

[44] B. A. Pickup and S. L. Thomson, “Flow-induced vibratory response of idealized versus magnetic resonance imaging-based synthetic vocal fold models,” *J. Acoust. Soc. Am.*, vol. 128, no. 3, p. EL124, 2010.

[45] R. J. Okamoto, E. H. Clayton, and P. V. Bayly, “Viscoelastic properties of soft gels: Comparison of magnetic resonance elastography and dynamic shear testing in the shear wave regime,” *Phys. Med. Biol.*, vol. 56, no. 19, pp. 6379–6400, 2011.

VITA

NAME:	Luca Leoni
EDUCATION:	Scientific High School Diploma (2010-2015), Liceo Scientifico Statale Leonardo Da Vinci, Milan, Italy
	Bachelor of Science in Biomedical Engineering (2015-2018), Politecnico di Milano, Milan, Italy
	Master of Science in Biomedical Engineering (2018-present), Politecnico di Milano, Milan, Italy
	Master of Science in Bioengineering (2019-present), University of Illinois at Chicago, Chicago, USA
WORK EXPERIENCE:	Research assistant (2020-present) for Richard and Loan Hill Department of Bioengineering, Acoustic and Vibrations Laboratory, University of Illinois at Chicago, Chicago, USA